

1 **Fully Coupled, High-Resolution Atmosphere-Ocean-Wave**  
2 **Simulations of the Offshore Wind Energy Environment During**  
3 **Hurricane Henri (2021)**

4 Chunyong Jung<sup>1</sup>, Pengfei Xue<sup>1,2,3</sup>, Chenfu Huang<sup>2,3</sup>, William Pringle<sup>1</sup>, Mrinal Biswas<sup>4</sup>, Geeta Nain<sup>1,2</sup>, and  
5 Jiali Wang<sup>1</sup>

6 <sup>1</sup>Environmental Science Division, Argonne National Laboratory, Lemont, IL 60439, USA

7 <sup>2</sup>Department of Civil and Environmental Engineering, Michigan Technological University, Houghton, MI 49931, USA

8 <sup>3</sup>Great Lakes Research Center, Michigan Technological University, Houghton, MI 49931, USA

9 <sup>4</sup>National Center for Atmospheric Research, Boulder, CO 80310, USA

10 *Correspondence to:* Chunyong Jung ([cjung2@anl.gov](mailto:cjung2@anl.gov)); Pengfei Xue ([pexue@mtu.edu](mailto:pexue@mtu.edu))

11

12 **Abstract.** A new fully coupled modeling system, integrating atmosphere, ocean, and wave models, is presented to simulate  
13 intricate interactions during tropical cyclones and explore their potential implications for offshore infrastructure. The system  
14 is evaluated on Hurricane Henri (2021), chosen for its distinctive track along the U.S. northeast coast, an area of densely  
15 populated regions and offshore wind energy zones. Three simulation setups are compared: atmosphere-only, atmosphere–  
16 ocean, and a fully coupled atmosphere–ocean–wave model. Among them, the fully coupled model produces the most realistic  
17 results, improving not only the storm intensity near the surface but also the wind structure from the near surface to the upper  
18 atmosphere. Waves enhance ocean surface cooling with an additional 0.5 K reduction via wave-induced vertical mixing and  
19 modify wind interactions through wave-driven surface roughness. This more realistic representation of coupled heat and energy  
20 exchanges between the atmosphere and ocean yield improved wind field patterns, which are critical for comprehensive risk  
21 assessment pertaining to offshore energy infrastructures. Furthermore, the coupled system reasonably captures wind-wave  
22 misalignment during the storm, with the greatest misalignment in the left-front and rear-left quadrants, while alignment occurs  
23 on the right side of the storm due to storm motion enhancing wave growth. These spatial variations highlight the need to  
24 accurately model atmosphere-ocean–wave interactions for reliable wind load assessments.

25

## 26 **1 Introduction**

27 Tropical cyclones (TCs) are among the costliest and deadliest natural hazards in the U.S., responsible for \$945.9 billion in  
28 damages and 6,502 fatalities from 1980 to 2019 (Smith, 2020). Although track forecasts have improved over recent decades,  
29 the ability to predict TC intensity remains limited (DeMaria et al., 2014; Rappaport et al., 2009; Yamaguchi et al., 2017; Zao  
30 et al., 2022). A key limitation lies in the incomplete representation of atmosphere-ocean interactions in models, particularly  
31 storm-induced sea surface temperature (SST) cooling (e.g., DeMaria et al., 2007; Zhao et al., 2017, 2022). This cooling is  
32 primarily driven by vertical mixing processes caused by strong TC-generated waves, intense upper-ocean shear, and upwelling  
33 associated with divergent ocean currents (Emanuel, 1986; Schade and Emanuel, 1999; Wu et al., 2016). While these air-sea  
34 interactions are recognized as critical drivers of storm intensity in a meteorological context, their implications for the offshore  
35 built environment remain insufficiently explored.

36 Current risk assessments conducted under hurricane conditions often simplify or omit these coupled feedback (e.g., Arthur,  
37 2021; Chen et al., 2024; Roldán et al., 2023; Sanchez Gomez et al., 2023), potentially leading to a disconnect between state-  
38 of-the-art numerical modeling and the practical evaluation of offshore structural vulnerabilities. One critical gap in current  
39 hurricane-focused offshore wind assessments is the impact of wind-wave misalignment on structural loads and potential  
40 damage. Such misalignment can significantly increase side-to-side turbine deflections and lead to underestimations of fatigue  
41 loads by as much as 50% in floating systems. For instance, a recent study by Shanahan and Fitzgerald (2025) found that wind-  
42 wave misalignment in floating offshore wind turbines can exceed 30° during hurricanes and reach up to ~58° along exposed  
43 western coastal zones of Ireland. Additionally, Ma and Sun (2023) used large-eddy simulations to model the coupled wind-  
44 wave loading on fixed-bottom offshore turbines, finding that under extreme events, such as hurricanes, aerodynamic loading  
45 increases: the mean bending moment at both tower and monopile rises by ~6%, the standard deviation of shear force increases  
46 by up to ~45%, and the bending movement variability increases by ~27%. These findings highlight the need for dynamic,  
47 coupled modeling approaches that can capture the evolving interactions among wind, waves, and currents, especially under  
48 extreme events, such as hurricanes (e.g., Chen et al., 2013; Barr and Chen., 2025).

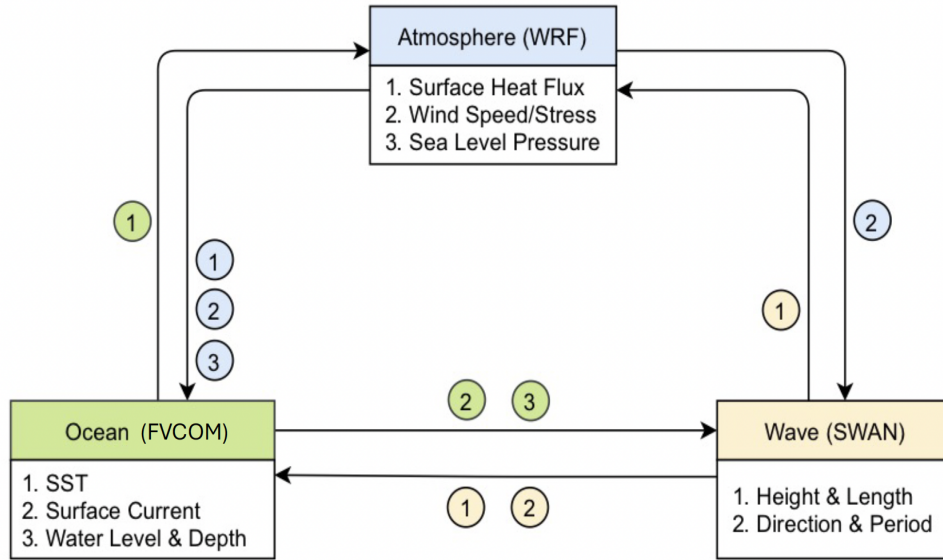
49 However, most current modeling frameworks used for wind energy risk assessment fall short in this regard. Uncoupled  
50 atmospheric models typically calculate surface roughness solely based on wind speed (e.g., via Charnock formulations),  
51 without explicitly representing wave-induced momentum fluxes (e.g., Sanchez Gomez et al., 2023), which can bias near-  
52 surface wind fields, shear profiles, and wind veer under extreme forcing. Statistical-parametric models, while efficient for  
53 probabilistic loss estimation, represent hurricane winds using idealized radial wind profiles—such as studies that use the classic  
54 Holland model (Arthur, 2021), the two-parameter Holland formulation (Chen et al., 2024), or recent asymmetric extensions  
55 (Roldán et al., 2023). By not explicitly accounting for the evolving feedback among wind, waves, and ocean currents, these  
56 approaches can underpredict or overpredict extreme gusts and rapid directional shifts that critically drive turbine loading.

57 To move beyond these idealized and uncoupled approaches, this study introduces a newly developed atmosphere-ocean-wave  
58 coupled modeling system that integrates a regional atmospheric mesoscale model with ocean and surface wave models, both

59 of which operate a high-resolution unstructured mesh. This framework, while sharing similarities with the Coupled Ocean  
60 Atmosphere Wave and Sediment Transport (COAWST; Warner et al., 2010), is distinguished by several key enhancements.  
61 First, it supports regional mesh refinement, allowing ultra-high resolution ocean grids over targeted areas such as offshore  
62 wind farms. This feature provides more localized and detailed oceanic information, improving the system’s utility for site-  
63 specific assessment. Second, our framework explicitly includes the effects of non-breaking wave processes in the coupling  
64 system. These processes, which require custom implementation (e.g., Xu et al., 2023), are not part of the standard COAWST  
65 model but are essential for realistically representing atmosphere-ocean-wave interactions, especially under extreme wind  
66 conditions such as those associated with TCs.

67 Within this modeling context, the present study focuses on characterizing the coupled offshore environmental forcing rather  
68 than on turbine-level structural response. While turbine loads and wake recovery are not directly explored, the study examines  
69 key aspects of atmosphere-ocean-wave interface that underpin such analyses. By assessing how coupling influences hub-height  
70 wind speeds and vertical wind profiles, this work provides relevant meteorological and oceanographical information that can  
71 inform future high-fidelity load modeling and offshore wind design studies and risk assessment. Accordingly, the primary  
72 objective of this study is to demonstrate the capabilities of the newly developed coupled framework and to evaluate its ability  
73 to resolve the complex atmosphere-ocean-wave processes that govern TC wind structure. We apply the system at high  
74 resolution (3 km for both atmospheric and oceanic components near the U.S. Northeast Coast) to Hurricane Henri (2021) as a  
75 case study. Henri was a Category 1 storm that made landfall in Rhode Island on 22 August 2021 and traversed the offshore  
76 wind energy lease area on the northeast continental shelf. Extensive observations, including airborne Doppler radar and  
77 dropsonde data near the eyewall, enable direct evaluation of modeled against observations. This study represents a necessary  
78 step toward transitioning offshore wind energy assessments from idealized or uncoupled parameterizations to a fully consistent,  
79 physics-based representation of environmental forcing under extreme weather conditions.

80 The development of the model, including detailed information on each model component and the coupler, is described in  
81 Section 2. Section 3 describes the experimental design and data used for model validation using Hurricane Henri (2021) as a  
82 working example. In Section 4 and 5, we present results and analysis, followed by the summary and discussions in Section 6.



83

84 **Figure 1. Schematic of coupled atmosphere-ocean-wave system and modelling used in this study.**

85 **2 Model Description**

86 The coupled atmosphere–ocean–wave modeling system integrates three core components: the Weather Research and  
 87 Forecasting (WRF) for atmospheric processes (V4.5.1; Skamarock et al., 2019), the Finite Volume Community Ocean Model  
 88 (FVCOM) for ocean circulation (V4.3.1; Chen et al., 2003, 2013), and the third-generation Simulating WAVes Nearshore  
 89 (SWAN) for wave dynamics (Booij et al., 1999), with data exchanged via a coupler (Fig. 1). Hereafter, we refer to the coupled  
 90 WRF-FVCOM-SWAN model as C-WFS. These components run in parallel and interact through the OASIS3-MCT coupler  
 91 (Craig et al., 2017). Details on each model, recent improvements, and the coupling strategy are provided in Sections 2.1–2.2.

92 **2.1 Model Components**

93 WRF is a nonhydrostatic, quasi-compressible atmospheric model featuring boundary layer physics and various sub-grid scale  
 94 parameterizations to simulate meso- and macroscale motions. In this study, we modified the WRF code to incorporate the  
 95 wave slope-based sea surface roughness formulation from Taylor and Yelland (2001) into several surface schemes, including  
 96 MYNN (Nakanishi and Niino, 2009; Olson et al., 2019) and both the original and revised MM5 schemes (Dyer and Hicks,  
 97 1970; Jimenez et al., 2012; Paulson, 1970; Webb, 1970):

98

99 
$$Z_0 = 1200H_s \left( \frac{H_s}{L_p} \right)^{4.5} + \frac{0.11v}{u_*} \quad Z_0 \leq 0.00285 \quad (1)$$

100

101 where  $Z_0$  is the surface roughness length,  $H_s$  is the significant wave height,  $L_p$  is the wavelength at the peak of spectrum,  $\nu$  is  
102 kinematic viscosity, and  $u_*$  is the friction velocity. Although C-WFS includes alternative wave-based formulations (e.g.,  
103 Drennan et al., 2003; 2005), our tests showed that the capped Taylor and Yelland (2001) method yielded the optimal  
104 performance for our case study.

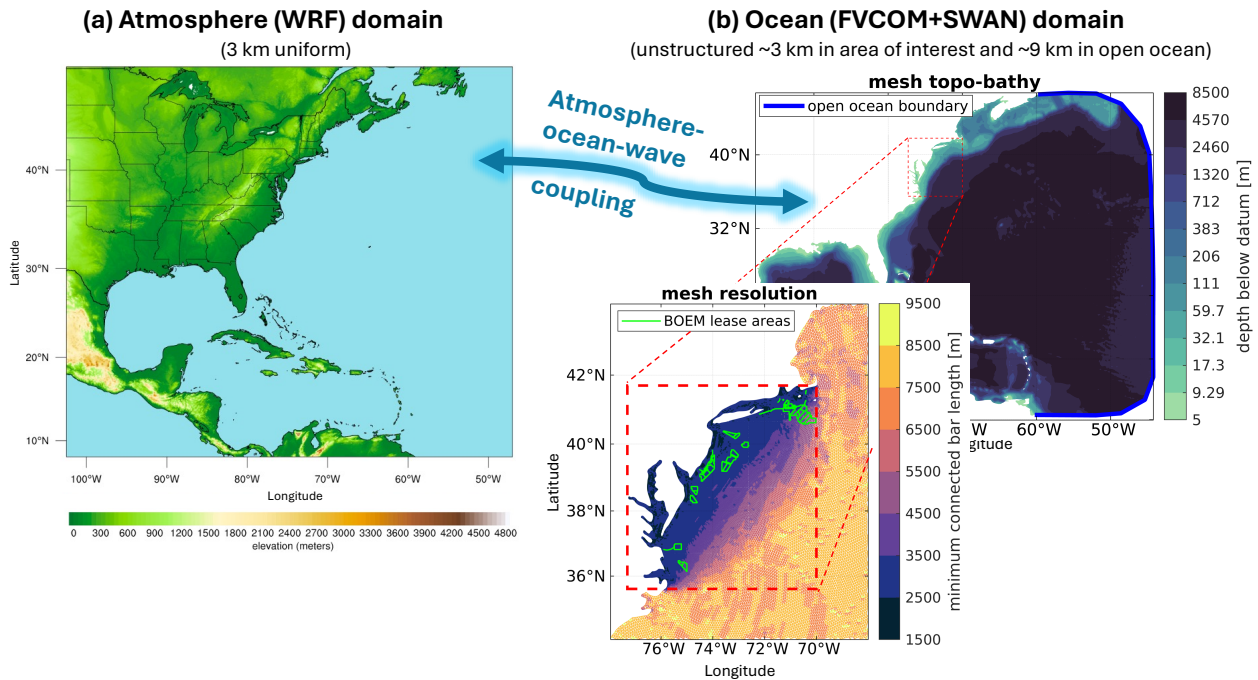
105 The ocean component, FVCOM (V4.3.1), is a 3D, free-surface, prognostic coastal circulation model that solves the primitive  
106 equations on an unstructured triangular grid using the finite-volume method. It enables dynamic interaction between ocean  
107 and atmospheric conditions throughout the simulation. In this study, we modified FVCOM to include vertical mixing induced  
108 by non-breaking waves, by adding a wave-related term to the turbulence eddy diffusivity  $B_v$ , following Ghantous and Babanin  
109 (2014a,b) and Aijaz et al. (2017):

$$110 \quad B_v = \alpha A^3 \kappa \sigma e^{3\kappa z} \quad (2)$$

111  
112 where  $\alpha = 0.1$ ,  $A$  = wave amplitude ( $H_s/2$ ),  $\kappa$  = wave number ( $2\pi/L$ ),  $\sigma$  = peak wave frequency ( $1/T_p$ ),  $z$  is water depth.  
113 The wave model component, SWAN v41.01, is a third-generation spectral wave model developed at Delft University of  
114 Technology that computes random, short-crested wind-generated waves in coastal regions and inland waters  
115 (<http://swanmodel.sourceforge.net/>). It solves the evolution equation of wave action density in space time, frequency and wave  
116 direction dimensions (Pringle and Kotamarthi, 2021). Various wave energy sources and sinks are modelled, including wave  
117 generation by wind, wave decay due to whitecapping, bottom friction, depth-induced wave breaking, and energy redistribution  
118 through nonlinear wind-wave interactions.  
119

## 120 **2.2 Coupler and Coupling**

121 OASIS3-MCT is a parallel coupler that synchronizes 2-D and 3-D field exchanges. Figure 1 outlines the C-WFS coupling  
122 framework and exchanged variables. WRF provides FVCOM with surface forcing—including friction velocity, winds, sea  
123 level pressure, heat fluxes, and radiation fluxes—while receiving SST from FVCOM as over-ocean boundary conditions. WRF  
124 also supplies wind fields to SWAN for wave simulations. In return, SWAN sends significant wave height and peak wavelength  
125 to WRF, which uses them to calculate sea surface roughness based on Equation 1. FVCOM uses wave fields from SWAN to  
126 compute radiation stress gradients, Stokes velocities, wave-enhanced bottom stresses, and non-breaking wave-induced mixing;  
127 breaking wave mixing is included via stress gradients. FVCOM also provides surface currents to SWAN, enabling Doppler  
128 shift effects from currents on wave behavior. This integrated coupling improves wave prediction accuracy by capturing wave-  
129 current interactions more realistically.



130

131

**Figure 2. (a) WRF model domain with terrain height elevation, and (b) FVCOM and SWAN domain with bathymetric depths and a zoom-in to the refined mesh grid along the northern U.S. East Coast and BOEM offshore lease areas.**

132

133

### 3 Application of C-WFS Modelling System

134

#### 3.1 Experimental Design and Configuration

135

To evaluate the integrated impact of ocean and wave processes on TC simulations, three experiments were performed. Experiment ‘A’ (atmosphere only) uses WRF with a 6-hourly updated SST. ‘AO’ couples WRF with FVCOM, enabling atmosphere-ocean interaction but no wave effects. ‘AOW’ fully couples WRF, FVCOM, and SWAN via OASIS3-MCT, allowing hourly, multi-way atmosphere-ocean-wave exchanges.

138

139

WRF is configured with a 3 km horizontal resolution and 46 vertical levels (12 below 100 m), covering much of the North Atlantic basin (Fig. 2a). It uses 6-hourly 0.25° NCEP (National Centers for Environmental Prediction) Global Forecast System (GFS; NCEP, 2015) analysis data for atmospheric initial and boundary conditions, with SSTs prescribed from GFS in ‘A’. The model employs WSM6 microphysics (Hong and Lim, 2006), RRTMG radiation (Iacono et al., 2008), Yonsei University PBL (Hong et al., 2006), and the Eta similarity surface layer scheme (Jimenez et al., 2012). No cumulus parameterization is used, as 4 km resolution or less supports convection-permitting simulations (Akisanola et al., 2024; Kouadio et al., 2020; Qing and Wang, 2021; Sun et al., 2016).

144

145

146

The ocean domain (FVCOM) covers most of the WRF domain, with horizontal resolution ranging from ~9 km in the open ocean to ~3 km over the continental shelf. It uses 40 sigma vertical layers to capture steep coastal bathymetry. Vertical mixing

147

148 processes are simulated using the Mellor–Yamada level-2.5 (MY25) turbulence closure model (Mellor and Yamada, 1982),  
149 and horizontal diffusivity is computed using the Smagorinsky numerical formulation (Smagorinsky, 1963). Initial and  
150 boundary conditions for currents, temperature, salinity, and water level are provided by 1/12° HYCOM (Hybrid Coordinate  
151 Ocean Model) analysis data (Cummings and Smedstad, 2014).

152 The wave model domain matches the FVCOM domain, using ~12 km horizontal resolution. The wave spectrum is divided  
153 into 36 directional and 24 frequency bins (0.04–1 Hz). Wave physics include Komen et al. (1984) for growth and whitecapping,  
154 Madsen et al. (1988) for bottom friction, and a constant depth-limiting breaker index, all with default settings. Swell boundary  
155 conditions are omitted due to minimal impact at the eastern boundary, and the model is initialized from a quiescent state.

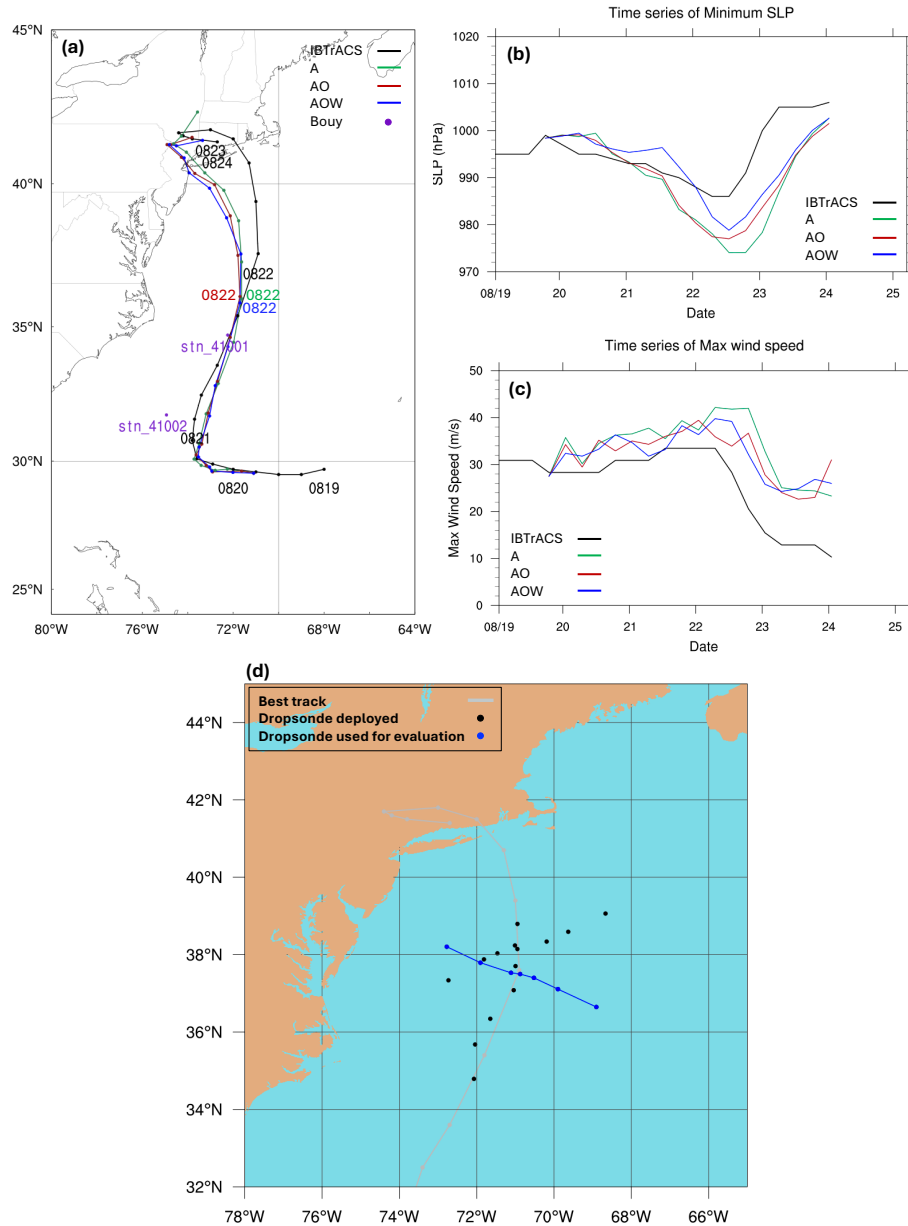
156 All experiments were initialized at 18:00 UTC on 19 August, 2021 and simulated for 102 hours. Nudging techniques were  
157 intentionally omitted to better isolate the effects of atmosphere–ocean–wave coupling on TC characteristics. Additional tests  
158 using various physics schemes and forcing datasets (e.g., ERA5) confirmed the robustness and low sensitivity of the results to  
159 model configuration choices, although the supporting results are not presented in this manuscript.

### 160 **3.2 Method and Data**

161 Model results are evaluated against several observational datasets, including International Best Track Archive for Climate  
162 Stewardship (IBTrACS; Knapp et al., 2010), which provides TC position, minimum sea level pressure (SLP), and maximum  
163 10-m sustained winds at ~6-hour intervals, and airborne observations. The airborne data include the Tropical Cyclone Radar  
164 Archive of Doppler Analyses with Recentering (TC-RADAR; Fischer et al., 2022) and dropsondes from NOAA’s Hurricane  
165 Research Division. TC-RADAR contains X-band Doppler radar data from NOAA’s WP-3D aircraft, scanning in front and  
166 back directions to produce detailed 3-D analyses of TC inner-core structure. Each mission typically includes 3–4 center passes,  
167 with storm-centered “recentering” techniques used to generate gridded analyses. Our simulations adopt the same storm-  
168 centered coordinates for direct comparison. A 300 km × 300 km grid is centered on the grid cell with minimum SLP in each  
169 dataset. To fill the 0–0.5 km altitude gap not captured by radar, we include dropsonde data. Due to slight differences in storm  
170 track and speed between the model and observations (Fig. 3), dropsonde positions are adjusted relative to the storm center  
171 (e.g., Creasey and Elsberry, 2017). Seven dropsondes (shown in Fig. 3d) from a single flight across the storm center were  
172 selected for evaluation; this flight crossed the storm from east to west within 50 minutes from 23:21 UTC on 21 to 00:11 UTC  
173 on 22 August 2020 (with exact times indicated in Fig 3d), 12 hours before peak intensity.

174 Modeled ocean surface waves are compared with observations from two National Data Buoy Center (NDBC, 2008) buoys,  
175 41001 and 41002, located on the left of the storm track on the continental slope. While there are more buoy locations, our  
176 focus is on the variation of storm-induced winds and waves along Henri’s track. We exclude stations near the U.S Northeast  
177 Coast due to the models’ track bias after 22 August (more discussion in Section 4). The buoy data provides surface wind and  
178 wave information, including surface wind speed, significant wave height, and peak wave period and direction. In addition to  
179 in-situ NDBC buoy measurements, we compiled a series of daily SST data from the Operational Sea Surface Temperature and

180 Ice Analysis (OSTIA; Good et al., 2020) at  $0.05^\circ \times 0.05^\circ$  resolution to determine the pre- and post-storm environment as well  
 181 as the difference between them.  
 182 The radius of maximum wind (RMW) defines the location of the maximum winds in a TC and is critical to understanding  
 183 intensity change as well as hazard impacts. In this study, we azimuthally average the vertical profiles of the seven dropsondes  
 184 and the simulations of wind speed relative to RMW to define the areas within and beyond the eyewall, allowing for a detailed  
 185 comparison of the storm's inner- and outer-core regions.



186

187 **Figure 3. Comparison of simulated (a) track, (b) minimum sea-level pressure (SLP), and (c) maximum 10-m wind speed of**  
188 **Hurricane Henri with IBTrACS Best Track data from 18 UTC 19 to 00 UTC 24 August 2021. Black lines show IBTrACS data;**  
189 **green, red, and blue lines represent experiments ‘A,’ ‘AO,’ and ‘AOW,’ respectively. Panel (d) shows the IBTrACS track (grey)**  
190 **with dropsonde positions (black and blue dots). The seven dropsondes shown as blue dots were released during a single NOAA**  
191 **WP-3D flight that traversed the storm center from west to east over approximately 50 minutes (23:21 UTC 21 to 00:11 UTC 22**  
192 **August). These dropsondes were used to evaluate model performance. Purple dots in (a) denote buoy stations 41001 and 41002**  
193 **from the National Data Buoy Center.**

## 194 **4 Model Validation**

### 195 **4.1 Track and Intensity**

196 Figure 3 presents the tracks, SLP minima, and surface wind speed maxima derived from the three simulations alongside  
197 IBTrACS. We emphasize at the outset that the purpose of this evaluation is not to assess forecast skill, but to provide a baseline  
198 comparison that enables interpretation of how atmosphere-ocean-wave coupling alters storm evolution and wind structure  
199 relative to partially coupled or uncoupled configurations.

200 The results indicate that variations in Henri's tracks across the three experiments show only minor differences (Fig. 3),  
201 consistent with previous findings suggesting that TC tracks are predominantly controlled by large-scale atmospheric circulation  
202 processes, rather than by atmosphere-ocean interactions at the temporal and spatial scales resolved in these models (e.g.,  
203 Zambon et al., 2014). The root-mean square error (RMSE, Table 1) of position indicates all three simulations have similar  
204 track errors, with values of 123.7 km for ‘A,’ 119.4 km for ‘AO,’ and 126.1 km for ‘AOW.’ Higher errors stem mainly from  
205 deviations after 00 UTC on 22 August, likely due to biases in midlatitude upper-level wave patterns (e.g., troughs and ridges)  
206 affecting the storm embedded in the baroclinic zone. While preliminary sensitivity tests indicate that spectral nudging can  
207 reduce track errors, nudging is intentionally excluded here to avoid constraining storm evolution and to better isolate the  
208 physical effects of atmosphere-ocean-wave interactions. All subsequent analyses therefore reflect unconstrained results.

209 In contrast to track, all three experiments overestimate storm intensity in terms of minimum SLP throughout most of Henri's  
210 lifecycle (Fig. 3b), particularly near peak at 12 UTC on 22 August. Nevertheless, systematic differences emerge among the  
211 experiments. Both ocean-coupled simulations (‘AO’ and ‘AOW’) reduce the magnitude of SLP overestimation relative to ‘A.’  
212 In ‘AOW,’ the overestimation of minimum SLP is delayed until 00 UTC on 22 August, after which it reaches the weakest peak  
213 minimum SLP among the three. This results in the lowest RMSE in minimum SLP (Table 1). These temporal trends also apply  
214 to the maximum surface wind speed (Fig. 3c and Table 1), demonstrating a reduction in overestimation of maximum surface  
215 wind speed in both ‘AO’ and ‘AOW’ compared to ‘A.’ Between the experiments ‘AO’ and ‘AOW,’ while ‘AOW’ generally  
216 exhibits weaker wind speeds compared to ‘AO,’ it becomes stronger as the storm approaches and reaches its peak intensity, in  
217 contrast to the findings for minimum SLP. This apparent decoupling between these two intensity metrics highlight the role of  
218 wave-modulated surface roughness and air-sea momentum exchange, and it motivates the mechanistic analysis presented in  
219 Section 5.

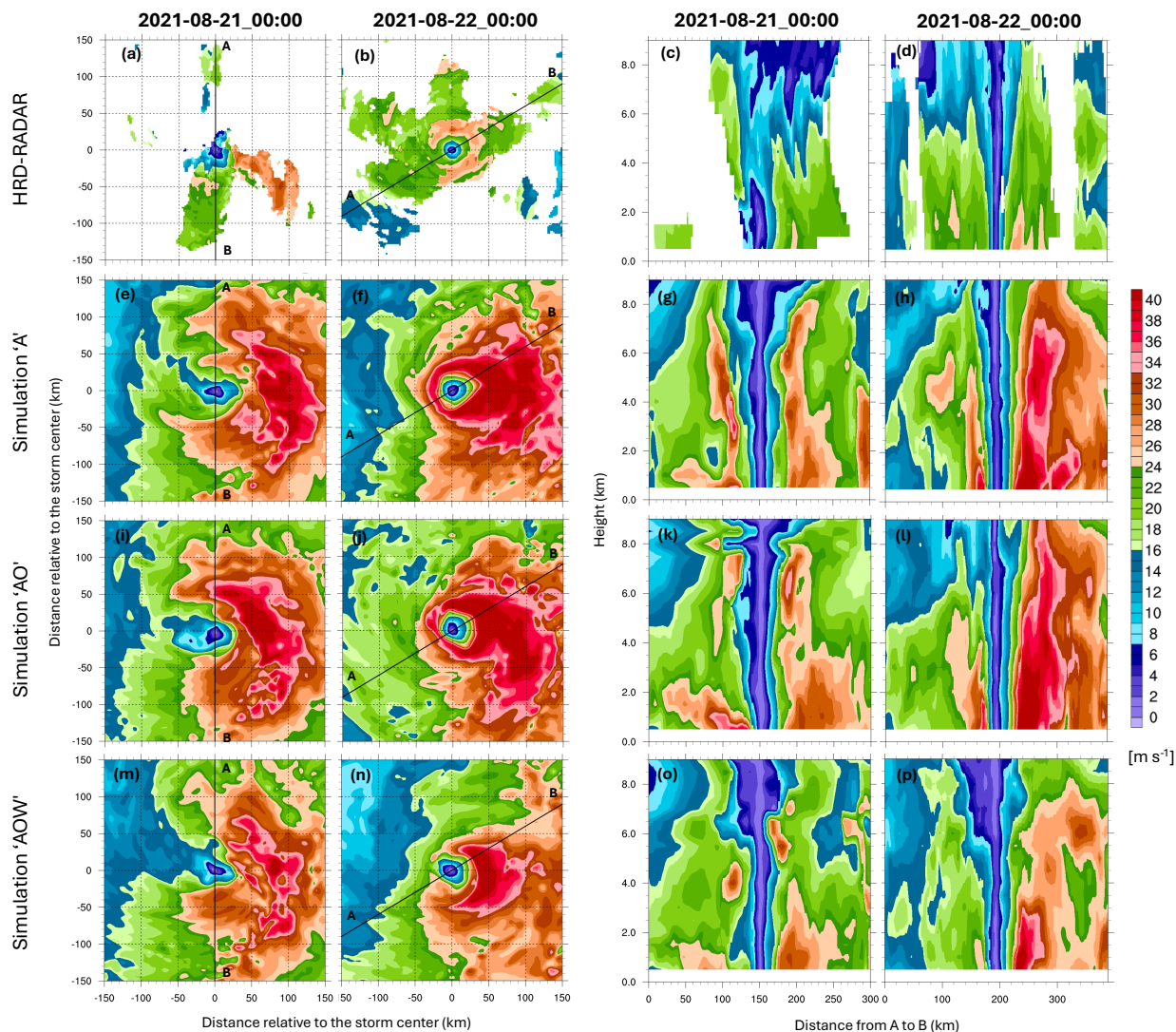
220 Overall, while the simulations exhibit clear deficiencies in. rack and intensity, the consistent and systematic differences among  
221 ‘A’, ‘AO’, and ‘AOW’ provide a useful framework for diagnosing how coupled ocean and wave processes influence storm  
222 structure. These relative differences—rather than absolute forecast accuracy—form the basis for the process-oriented analysis  
223 that follows.

224

225 **Table 1. Root mean square error (RMSE) for each simulation in terms of minimum sea level pressure (hPa), maximum surface wind**  
226 **speed ( $\text{m s}^{-1}$ ), and cyclone track (km).**

Experiment	Min. sea level pressure (hPa)	Max. surface wind speed (m/s)	Cyclone track (km)
A	9.4	10.2	123.7
AO	7.9	8.7	119.4
AOW	6.4	8.3	126.1

227



228

229 **Figure 4.** NOAA WP-3D airborne Doppler radar (TC-RADAR) wind speeds at the 1-km level are shown in the top row, with model-  
 230 simulated wind speeds from the ‘A’ (second row), ‘AO’ (third row), and ‘AOW’ (fourth row) simulations of Hurricane Henri (2021)  
 231 at 00 UTC on 21 (first and third columns) and 22 August (second and fourth columns). Vertical cross-sections along the A–B line  
 232 (marked in the left two panels) are shown in the right two columns. All horizontal fields are plotted in a  $300 \times 300$  km storm-centered  
 233 domain.

## 234 4.2 Storm Wind Structure

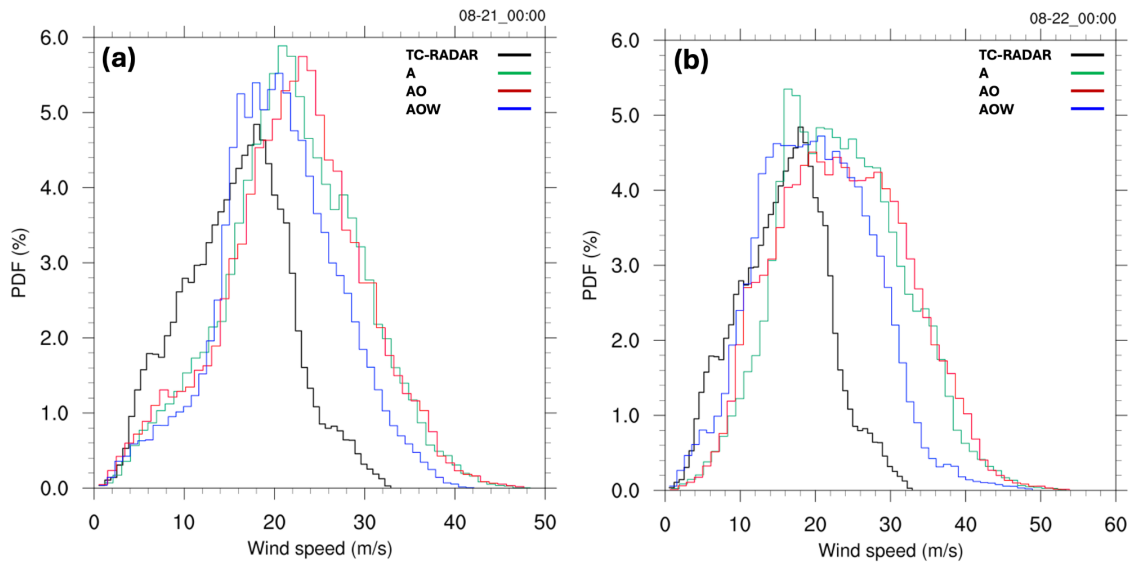
235 Figures 4a–d show 1-km level wind speeds and vertical profiles from TC-RADAR at 00 UTC on 21 and 22 August 2021,  
 236 along the black lines in Figs. 4a–b. On 21 August, observations reveal a strongly asymmetric wind field, with the highest winds  
 237 concentrated on the storm's right side. This asymmetry results from the combination of Henri's cyclonic circulation and its  
 238 poleward motion, which enhances wind speeds on the right through additive forward momentum. The vertical cross-section

239 (Fig. 4c) along line A–B shows wind speeds  $>20 \text{ m s}^{-1}$  largely confined below 4 km on the southern side but extending to 8 km  
240 on the northern side. By 00 UTC on 22 August, 12 hours before its minimum central pressure, Henri’s wind field becomes  
241 more symmetric and compact, with a closed eyewall and winds exceeding  $24 \text{ m s}^{-1}$  (Figs. 4b,d). A clear calm zone is evident  
242 within the eyewall, extending up to 9 km. Strong winds are more evenly distributed around the center, but remain strongest on  
243 the right. Corresponding model-simulated wind profiles and 1-km level horizontal wind fields at both times are shown in Figs.  
244 4e–p.

245 All three simulated storms reasonably capture Henri’s structural evolution—from a broad, asymmetric wind pattern with strong  
246 right-side winds at 00 UTC 21 August (as seen in TC-RADAR) to a more compact, symmetric structure by 00 UTC 22 August.  
247 However, the simulations, especially experiments ‘A’ and ‘AO,’ overestimate wind intensity both horizontally and vertically.  
248 The fully coupled run ‘AOW’ reduces this bias, producing more realistic radial wind profiles at 1 km along line A–B (Fig. S1)  
249 and achieving the highest Pearson correlations with TC-RADAR ( $r = 0.95$  for horizontal distribution and  $0.72$  for vertical  
250 cross-section). To assess wind distribution more comprehensively, we use probability density functions (PDFs) across all  
251 available TC-RADAR grid cells (0.5–9 km altitude within a  $300 \times 300 \text{ km}$  domain centered on the storm). All simulations  
252 skew toward higher wind intensities, but ‘AOW’ shows improved performance, especially in the upper tail, suggesting reduced  
253 wind bias during storm intensification (Fig. 5).

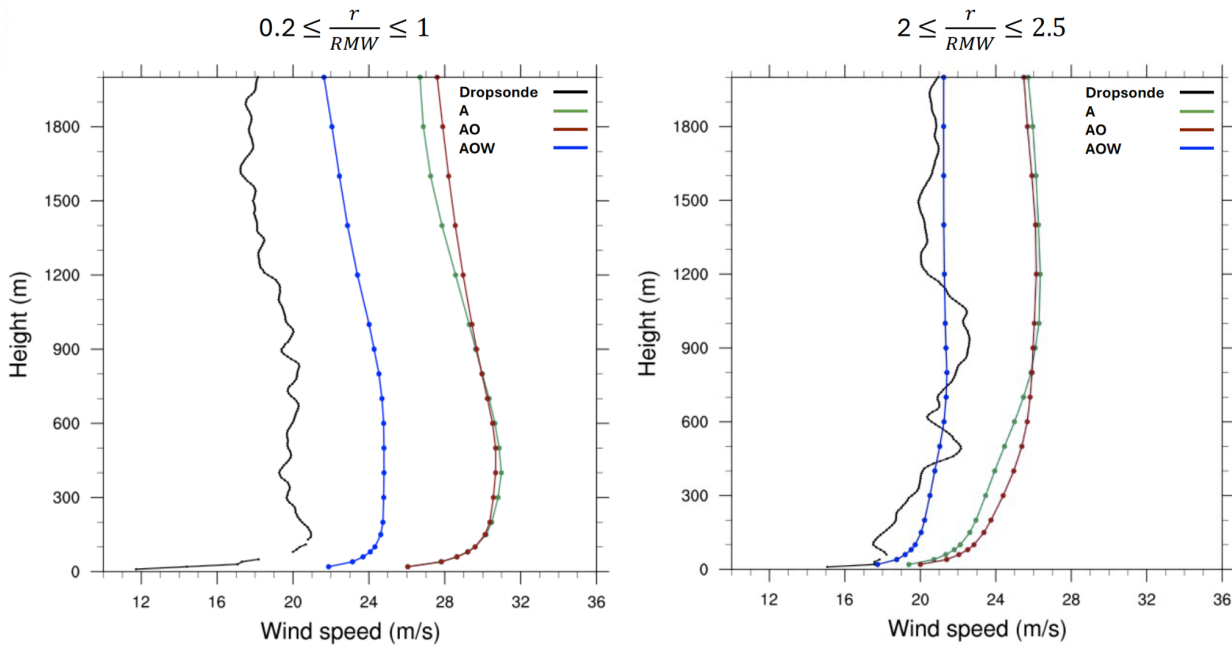
254 While TC-RADAR provides rich horizontal and vertical coverage, it only samples above 0.5-km, limiting surface-level  
255 validation. Dropsonde data help bridge this gap. Figure S2 shows vertical cross-sections up to an altitude of 3.2 km along the  
256 blue line in Fig. 3d: consistent with TC-RADAR, strongest winds appear 10–30 km east of the center, while much weaker  
257 winds dominate the western side. These asymmetries are captured in all simulations, though generally overestimated.

258 Azimuthally averaged vertical profiles (Fig. 6) in the inner-eyewall ( $0.2 \leq r/\text{RMW} \leq 1$ ) and outer-eyewall ( $2 \leq r/\text{RMW} \leq 2.5$ )  
259 regions at the dropsonde locations further confirm that all simulations overestimate low-level winds (below 2 km). However,  
260 ‘AOW’ aligns more closely with observations, particularly in the outer-eyewall. This improvement is critical, as it provides  
261 the necessary baseline environmental forcing for offshore wind energy studies, including high-fidelity load modeling and risk  
262 assessment in storm-prone regions.



263

264 **Figure 5:** Probability density function of wind speed in a 300 km x 300 km storm-centered coordinate, considering vertical levels  
 265 from 0.5 km to 9 km above the ground, for 00 UTC on 21 (a) and 22 August (b) 2021. The data are derived from TC-RADAR (black  
 266 lines), experiment 'A' (green lines), experiment 'AO' (red lines), and experiment 'AOW' (blue lines).



267 **Figure 6.** Vertical profiles of azimuthally averaged wind speed for dropsondes (black lines), experiment 'A' (green lines), experiment  
 268 'AO' (red lines), and experiment 'AOW' (blue lines). The vertical profiles are azimuthally averaged in the inner-eyewall region (left;  
 269  $0.2 \leq r/RMW \leq 1$ ) and the outer-eyewall regions (right;  $2 \leq r/RMW \leq 2.5$ ), based on the locations of the seven dropsondes highlighted  
 270 in blue dots in Fig. 3d at 00 UTC on 22 August 2021. RMW indicates radius of maximum wind, and r shows radius relative to the  
 271 storm center.  
 272

### 273 4.3 Sea Surface Temperature

274 From the ocean’s perspective, SST and surface roughness are key factors influencing TC intensity, as they directly affect the  
275 exchange of heat, moisture, and momentum between the ocean and the storm (Zambon et al., 2014, 2021; Zhao et al., 2022).  
276 The main distinction among the three simulations lies in how SST and ocean surface roughness are represented, influencing  
277 surface enthalpy and momentum fluxes through air-sea interactions. Accordingly, SST is used both as an indicator of storm  
278 evolution and as a dynamic driver of intensity across the three simulations. Therefore, evaluating how well the coupled model  
279 reproduces observed SST is critical for assessing its ability to realistically capture ocean dynamics and storm–ocean  
280 interactions.

281 Figure 7 shows the SST distribution across the simulation domain for all three experiments, along with OSTIA observations  
282 from 12 UTC on 20 to 12 UTC on 23 August 2020. Since OSTIA provides daily SST data, the statistics in Table 2 represents  
283 an average over these four days. In experiment ‘A’, the SST is derived from GFS, and is technically driven by observed SST  
284 data. Therefore, it captures key large-scale features well, such as the Gulf Stream and warm waters along the Gulf Coast.  
285 However, it consistently underestimates SST across the domain during this period. In addition, its relatively low resolution  
286 ( $0.25^\circ$ ) limits its ability to capture small-scale SST patterns, contributing to the higher RMSE values shown in Table 2.

287 The ocean-coupled simulations ('AO' and 'AOW'), which are driven by oceanic initial and boundary conditions from the  
288 HYCOM analysis, successfully capture major SST features such as the Gulf Stream and Gulf Coast, with enhanced spatial  
289 detail. This improved representation contributes to lower RMSE values compared to the atmosphere-only simulation ('A')  
290 (Table 2). However, both 'AO' and 'AOW' tend to overestimate SSTs in the open North Atlantic and underestimate them near  
291 the northeastern U.S. coast (Figs. 7d, l, p), likely due to cold wakes generated by the simulated storms and deviations in their  
292 tracks from observations. Nevertheless, the ocean-coupled simulations reasonably reproduce the observed SST, with RMSE  
293 values of 0.564 and 0.577 for ‘AO’ and ‘AOW’, respectively—lower than that of 'A'—while maintaining comparable pattern  
294 correlation overall (Table 2).

295 To assess the potential influence of track biases on SST and MSLP, we first examined 'A' simulation. It exhibits  
296 overintensification of MSLP, a consequence of its simulated track failing to coincide with the observed cold wakes in the GFS  
297 data. This misalignment prevents the realistic capture of crucial atmosphere-ocean heat and moisture exchanges. Conversely,  
298 ocean-coupled simulations ('AO' and 'AOW') more accurately represent storm-induced modifications to surface energy and  
299 momentum fluxes. By explicitly modeling SST cooling along their simulated storm paths, these coupled runs achieve a more  
300 realistic depiction of storm intensity. In particular, 'AOW' simulation shows enhanced SST cooling around the time of peak  
301 intensity and thereafter, further contributing to a reduction in MSLP. Spatial and temporal averaging of SST within a  $300\text{ km} \times 300\text{ km}$   
302 storm-centered domain from 12 UTC on 21 August to 12 UTC on 22 August indicates an SST of 299.7 K for ‘AOW’,  
303 compared to 300.2 K previously—representing a 0.5 K reduction and bringing it closer to the OSTIA value of 299.1 K (Table  
304 3). Details of the storm-centered SST distributions are provided in the Supplementary Information (Fig. S3). This improved  
305 performance in 'AOW' can be attributed to the effect of wave-induced vertical mixing, which effectively brings cooler

306 subsurface water to the surface, aligning with our previous discussion and prior research (e.g., Wada et al., 2010; Zambon et  
307 al., 2014)

308

309 **Table 2. Temporally averaged root mean square error (RMSE) and Pearson product- moment coefficient of linear correlation (r)**  
310 **for SST in each simulation compared to OSTIA SST observations from 12 UTC on 20 to 12 UTC 23 August, 2021.**

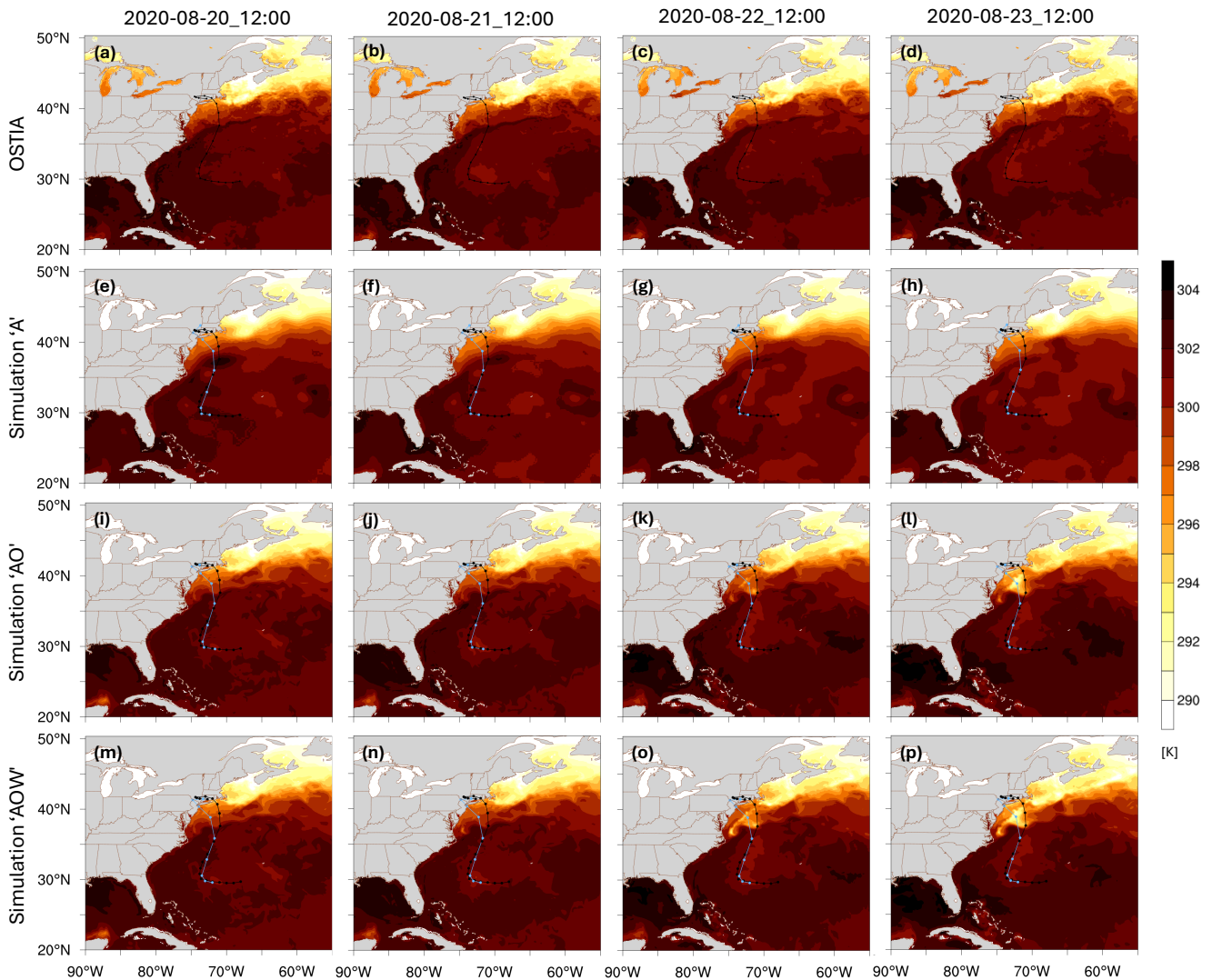
Experiment	RMSE	Pattern Correlation
A	0.631	0.992
AO	0.564	0.991
AOW	0.577	0.990

311

312 **Table 3. Spatially averaged SST (K) derived from A, AO, AOW, and OSTIA observation in a 300 km x 300 km storm-centered**  
313 **coordinate at 12 UTC 20, 12 UTC 21, and 12 UTC 22 August.**

Experiment	12 UTC 20 August	12 UTC 21 August	12 UTC 22 August
A	302.01	301.81	299.37
AO	301.79	301.83	298.47
AOW	301.76	301.70	297.70
OSTIA	302.15	301.43	296.76

314



315

316 **Figure 7. SST distribution (K) for OSTIA (top row), 'A' (second row), 'AO' (third row) and 'AOW' (bottom row) at 12 UTC on 20**  
 317 **(first column), 21 (second column), 22 (third column), and 24 August 2020 (fourth column). The black dots and lines indicate the**  
 318 **best track derived from IBTrACS. The light blue dots and lines depict simulated storm locations and tracks.**

#### 319 **4.4 Ocean Surface Waves**

320 This section assesses how accurately our model simulates ocean surface waves during Hurricane Henri at two NDBC buoy  
 321 locations. During Henri's primary development, buoy 41001 was directly in the path of the eyewall, while buoy 41002 was  
 322 positioned approximately 120 km to the left of the storm's center during its earlier stages (Fig. 3a). The fully coupled  
 323 experiment successfully captures the general temporal trends in wind speed at both sites (Figs. 8a–b). However, a slower  
 324 simulated storm translation speed, particularly between 06:00 and 12:00 UTC on 21 August, led to a delay of roughly 12 hours  
 325 in both wind speed and wave height peaks. Furthermore, the model overestimates significant wave height by about 1–2.5 m at

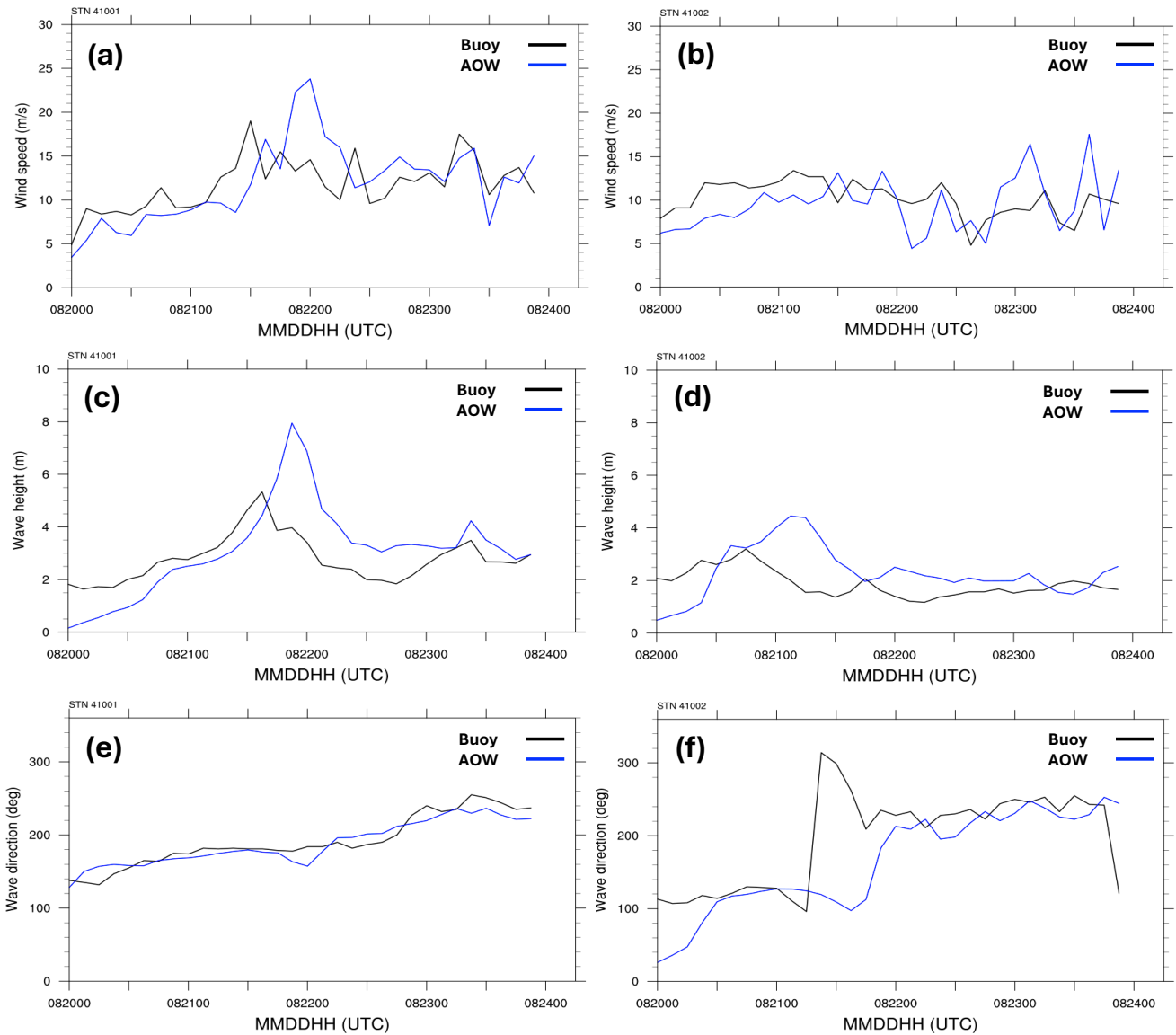
326 both locations during peak conditions (Figs. 8c–d). At station 41001, this overestimation is primarily attributable to  
327 discrepancies in wind speed. For station 41002, an additional contributing factor is the model's faster simulated translation  
328 speed— $6.3 \text{ m s}^{-1}$  compared to the observed  $4.8 \text{ m s}^{-1}$  between 00:00 and 06:00 UTC on 21 August. It is well-established that  
329 increased forward motion enhances wind speed and wave growth on a storm's right side, leading to higher waves (Chen et al.,  
330 2013). While the model accurately reproduces wave direction at station 41001, it fails to capture the sharp directional shift  
331 observed at station 41002 between 06:00 and 09:00 UTC on 21 August (Figs. 8e–f). This discrepancy may stem from the  
332 model's increased wave height and wavelength, which can suppress rapid directional changes. Despite these biases in wave  
333 height magnitude and timing, the model generally provides a reasonable representation of wave behavior at both locations and  
334 successfully captures key trends in storm-induced wave dynamics during Hurricane Henri.

335 Understanding the accuracy of modeled ocean surface waves, particularly their directional characteristics, is crucial because  
336 previous investigations into TC wind impacts on offshore wind turbines (e.g., Sanchez Gomez et al., 2023; Wei et al., 2017;  
337 Itiki et al., 2023) have often relied on atmosphere-only frameworks or empirical wave representations. As noted in several of  
338 those studies such approaches necessarily simplify or exclude explicit wind-ocean-wave coupling processes, which may  
339 influence both direct and indirect load pathways. These acknowledged modeling limitations motivate the need for coupled  
340 approaches that better represent wind-wave interactions when assessing offshore wind risk extreme conditions. For instance,  
341 Ma and Sun (2023) demonstrated that under extreme wind-wave conditions, such as those in hurricanes, coupling between  
342 wind and wave dynamics significantly increases the aerodynamic loads on offshore wind turbines. This coupling markedly  
343 amplifies the variability of those loads, suggesting that traditional decoupled models may underestimate the structural demands  
344 during such severe events.

345 Figure 9 shows that wind and wave alignment varies considerably over time, with periods of near co-alignment interspersed  
346 with misalignments. The directional divergence is site-specific, highlighting the influence of localized impact depending on  
347 locations relative to the storm center. 'AOW' captures key characteristics of directional interactions, reproducing the timing  
348 and magnitude of misalignment trends reasonably well (Figs. 9 bottom panel). Notably, the simulations capture the directional  
349 sensitivity at both sites, suggesting fidelity in representing storm-induced wave generation and propagation. By resolving wind-  
350 wave misalignment, the fully coupled modeling system provides a more physically consistent description of the environmental  
351 conditions relevant to offshore infrastructure under extreme events such as TCs.

352 Figure 10 illustrates simulated ocean surface wave conditions and 10-m wind vectors from 'AOW' experiment at 12:00 UTC  
353 on 22 August. Consistent with prior studies (e.g., Chen et al., 2013; Wright et al., 2001), TC-induced wave fields typically  
354 exhibit asymmetry, with the highest significant wave heights occurring in the front-right quadrant. This pattern is clearly  
355 evident in our simulation, as Henri moves northwest, producing the largest waves in its right and front-right quadrants (Fig.  
356 10a). The storm's motion further enhances wave growth on the right side due to a longer fetch (Figs. 10a–b). Significantly,  
357 directional misalignment between wind and waves is apparent across most storm quadrants, except on the right side where  
358 both wind and waves are aligned, also consistent with previous findings (Fig. 10d). This widespread misalignment as well as

359 aligned directions highlight the complex atmosphere-wave interactions that necessitate careful consideration in offshore wind  
360 load assessments.



361  
362 **Figure 8. Comparison of the 'AOW' simulation (blue) with observations (black) for Hurricane Henri from 00 UTC 20 to 00 UTC 24**  
363 **August 2021: (a–b) wind speed (m/s), (c–d) significant wave height (m), and (e–f) wave direction. The right column shows data from**  
364 **station 41001, while the left column depicts station 41002. The locations of stations 41001 and 41002 are shown in Figure 3(a).**

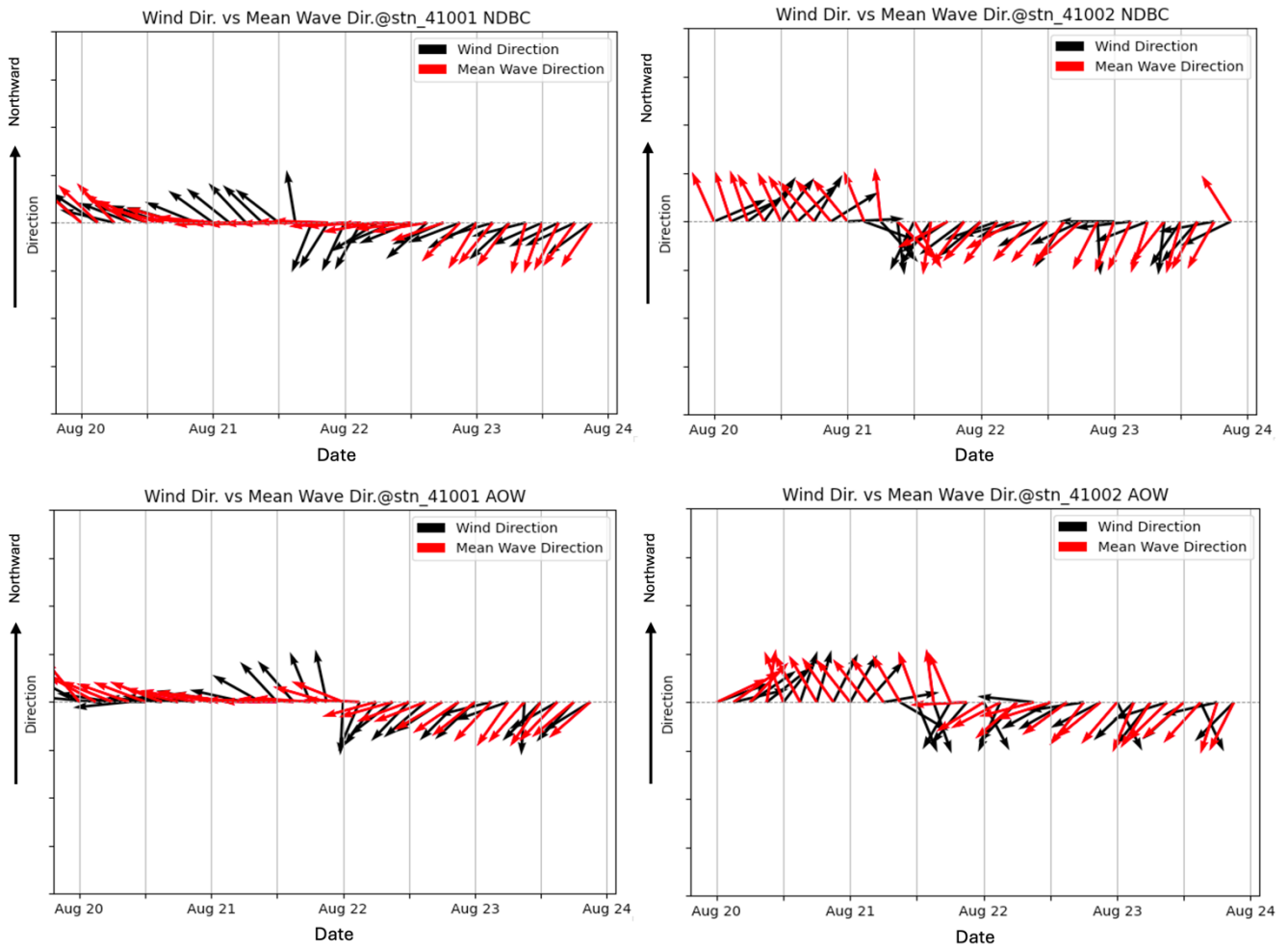
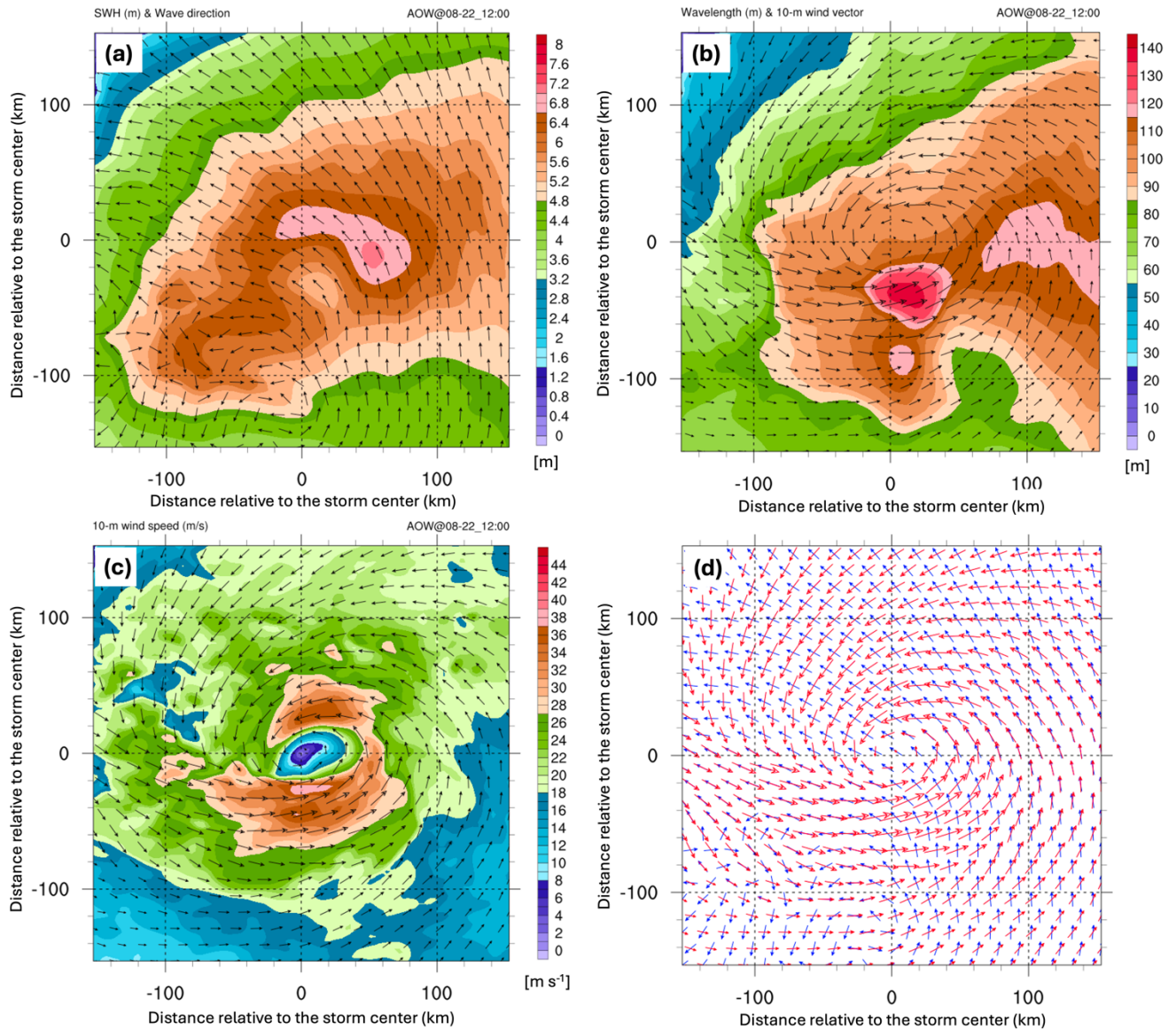


Figure 9. Time series comparison of surface wind direction and mean ocean surface wave direction at two NDBC buoy stations, 41001 (left column) and 41002 (right column), derived from NDBC buoys (top panel) and experiment 'AOW' (bottom panel).

365  
 366  
 367  
 368



369  
 370 **Figure 10.** The fully coupled model output at 12 UTC on 22 August 2021 includes: (a) significant wave height (shaded; in meters)  
 371 and wave direction, (b) mean wavelength (shaded; in meters) and 10-m wind, (c) 10-m wind speed (shaded; in m/s) and vectors, and  
 372 (d) wave (blue) and wind (red) vectors. All plots are in a 300 × 300 km storm-centered domain, with a 20 m/s reference wind vector  
 373 shown in panels (b) and (c).

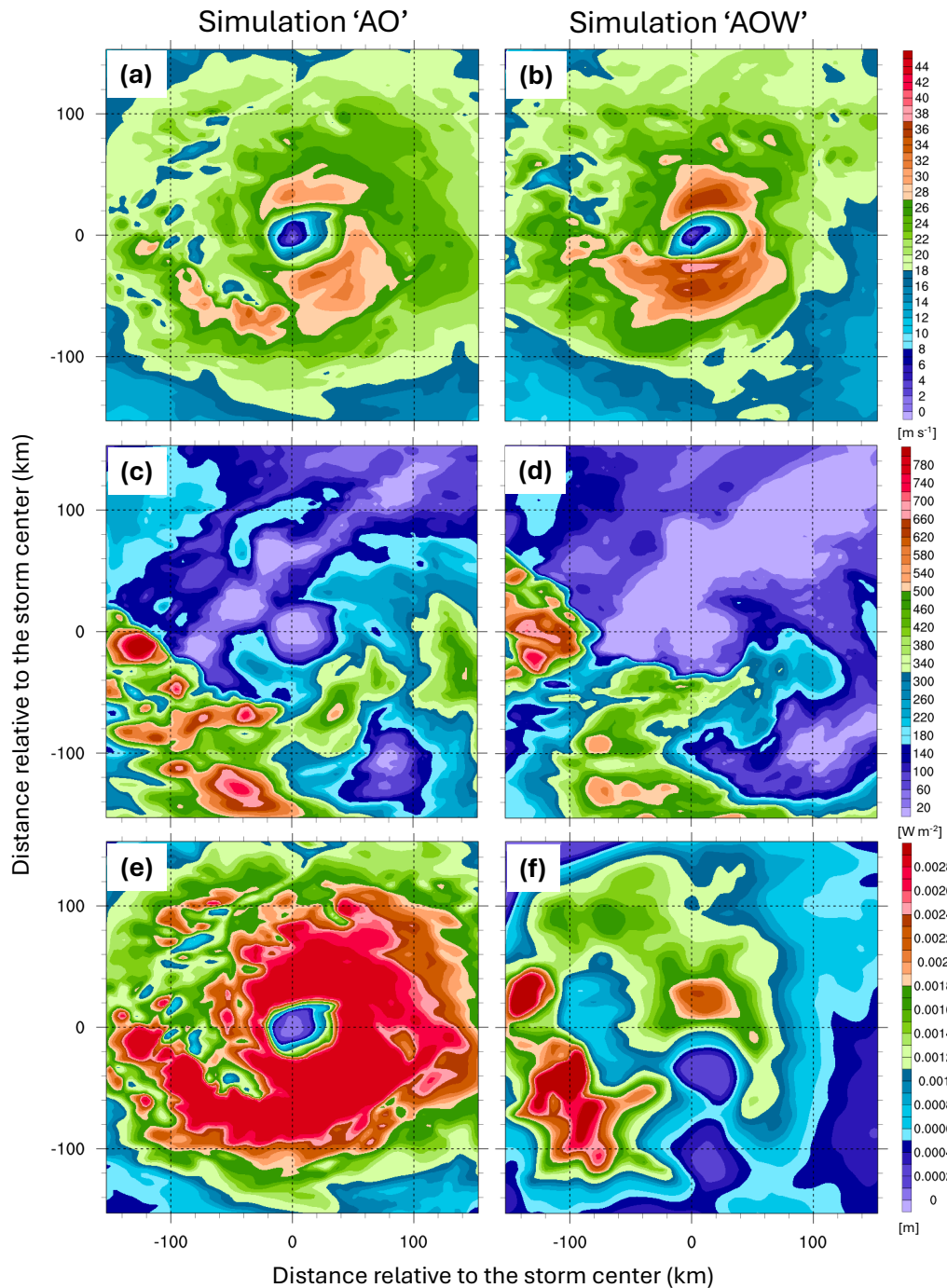
### 374 5 Mechanisms Underlying the Improvement in the Fully Coupled Experiment

375 Compared to experiments ‘A’ and ‘AO’, ‘AOW’ reduces the overestimation of storm intensity (minimum SLP; Fig. 3) and  
 376 improves the storm-scale wind structure (Fig. 4), PDF distribution (Fig. 5), and profiles (Fig. 6) from the near surface to the  
 377 upper troposphere. To understand these improvements, we analyze SST and surface enthalpy fluxes in ‘AOW’ versus ‘AO’ to

378 assess the role of wave-induced processes in Henri’s evolution. Experiment ‘A’ is excluded since it is atmosphere-only and  
379 lacks atmosphere–ocean interactions.

380 Because ‘AO’ and ‘AOW’ have very similar storm tracks and translation speeds, we can isolate surface processes—SST,  
381 enthalpy flux, and surface roughness length ( $Z_0$ )—to evaluate their impact on storm intensity and evolution. In ‘AOW’, ocean  
382 surface waves affect  $Z_0$ , which regulates momentum, heat, and moisture exchange at the air–sea interface. In uncoupled  
383 simulations like ‘AO’,  $Z_0$  follows Charnock’s formulation and depends only on wind speed, with no explicit dependence on  
384 wave-state properties. This limits capturing dynamic air–sea interactions during TCs, where sea state significantly influences  
385 momentum transfer and storm development. Focusing on 12 UTC, 22 August—about 12 hours before landfall when both  
386 simulations reach peak minimum SLP—reveals notable differences in  $Z_0$  distribution (Fig. 11). In ‘AO’, the distribution and  
387 strength of  $Z_0$  closely follow the surface wind speed through the Charnock relation. In contrast, ‘AOW’ simulation shows a  
388 different  $Z_0$  pattern (e.g., Taylor and Yelland, 2001; Drennan et al., 2005; Shimura et al., 2017), with reduced values driven by  
389 wave dynamics, highlighting the significant role of waves in modulating air–sea momentum and energy exchange (Figs. 11a–  
390 b, e–f). Prior studies have shown that drag coefficient ( $C_d$ ) saturates or even decreases once wind speeds exceed approximately  
391 30–35  $\text{m s}^{-1}$ , largely due to wave processes which dampen momentum transfer to the ocean (e.g., Donelan et al., 2004; Powell  
392 et al., 2003). Since surface roughness length ( $Z_0$ ) is directly correlated with  $C_d$  via Monin-Obukhov theory, this saturation  
393 implies a corresponding weakening or plateauing of surface roughness.

394 The influence of ocean surface waves extends beyond modifying  $Z_0$ . Although ‘AOW’ exhibits stronger winds, it also shows  
395 lower SST and reduced surface enthalpy flux compared to ‘AO’ (Figs. 7l,p, and 11c-d). The primary driver of SST cooling  
396 under TCs is ocean vertical mixing. Storm-induced surface winds generate frictional stress, which drives upper-ocean currents  
397 and promotes evaporation. Vertical shear in these currents produces turbulence that mixes cooler subsurface water into the  
398 mixed layer, reducing SST (e.g., Zhou et al., 2023). This process occurs in both ‘AO’ and ‘AOW’. However, ‘AOW’ introduces  
399 additional vertical mixing through wave dynamics. As surface winds generate waves, momentum is transferred into the ocean.  
400 Breaking waves inject momentum deeper, enhancing shear and mixing. Long period, large wave height non-breaking waves  
401 that are generated by TCs further deepen the vertical mixing, amplifying SST cooling. These wave-induced processes in ‘AOW’  
402 lead to cooler SSTs and lower enthalpy fluxes than in ‘AO’ (Fig. 11). Additionally, the reduced  $Z_0$  in ‘AOW’ corresponds to  
403 a lower  $C_d$  resulting in less surface roughness and higher near-surface wind speeds due to the inclusion of wave effects.



404  
 405 **Figure 11.** Distribution of (a)-(b) 10-m wind speed ( $\text{m s}^{-1}$ ), (c)-(d) surface enthalpy flux ( $\text{W m}^{-2}$ ), and (e)-(f) surface roughness length  
 406 (m) derived from the experiment 'AO' (left column) and the experiment 'AOW' (right column) at 12 UTC on 22 August 2021. All  
 407 distributions are displayed in a  $300 \text{ km} \times 300 \text{ km}$  storm-centered coordinate.  
 408

409 An important question remains regarding the discrepancy between minimum SLP and maximum wind speed in ‘AO’ and  
 410 ‘AOW’ simulations. Although ‘AO’ produces a lower minimum SLP, it shows weaker maximum wind speeds than ‘AOW’—  
 411 despite higher surface enthalpy and momentum fluxes at peak intensity (12 UTC, 22 August; Figs. 3b–c, 11a–b). As discussed,  
 412 this is due in part to the higher  $Z_0$  in ‘AO’, resulting from the absence of wave dynamics. Increased  $Z_0$  leads to greater frictional  
 413 drag, reducing near-surface wind speeds. This enhanced friction contributes to stronger subgradient winds, where actual wind  
 414 speeds fall below those expected from gradient wind balance. The imbalance between forces in the boundary layer is described  
 415 by the agradient force (AF), defined as:

$$416$$

$$417 \quad \text{Agradient Force (AF)} = -\frac{1}{\rho} \frac{\partial p}{\partial r} + \frac{V_t^2}{r} + fV_t \quad (3)$$

418

419 where  $p$  is pressure,  $r$  is the radial distance from the TC center,  $V_t$  is the tangential wind speed,  $\rho$  is air density, and  $f$  is the  
 420 Coriolis parameter. Near the surface, both ‘AO’ and ‘AOW’ deviate from gradient wind balance due to friction, which reduces  
 421  $V_t$ , weakening both the Coriolis and centrifugal forces. With the pressure gradient force unchanged, this creates a negative  
 422 agradient force ( $AF < 0$ ), driving radial inflow. This inflow forms part of the storm’s secondary circulation. Its strength can  
 423 indicate the degree of deviation from gradient wind balance—stronger inflow implies greater subgradient winds. Table 4  
 424 clearly shows that ‘AO’ is associated with a stronger surface pressure gradient force, which, along with a higher  $Z_0$ , creates  
 425 more favorable conditions for enhanced mass flux inflow. On the other hand, ‘AO’ exhibits weaker absolute angular  
 426 momentum (AAM), defined as:

$$427$$

$$428 \quad M = rV_t + \frac{1}{2}fr^2 \quad (4)$$

429

430 As shown in Equation 4, AAM is closely tied to the storm’s rotational wind structure. Therefore, to better understand the  
 431 discrepancy between ‘AO’ and ‘AOW’—specifically why ‘AO’ has a stronger pressure gradient but weaker winds—we  
 432 analyze the AAM budget, following Zhang and Marks (2015) and Zhao et al. (2022). The AAM budget equation used is:

$$433$$

$$434 \quad \frac{\partial \langle M \rangle}{\partial t} = -\langle V_r \rangle \frac{\partial \langle M \rangle}{\partial r} - \langle w \rangle \frac{\partial \langle M \rangle}{\partial z} - \langle V_r' \rangle \frac{\partial M'}{\partial r} - \langle w' \rangle \frac{\partial M'}{\partial z} + F_r \quad (5)$$

435

436 where  $V_r$  and  $w$  denote radial wind speed and vertical wind component, respectively. Brackets  $\langle \rangle$  denote azimuthal averages,  
 437 and primes indicate deviations from the mean. The left-hand side represents the time tendency of azimuthally averaged AAM.  
 438 The right-hand side includes contributions from mean radial advection, mean vertical advection, radial eddy transport, vertical  
 439 eddy transport, and friction/residual term  $F_r$ . We hypothesize that the higher  $Z_0$  in ‘AO’—a result of the simplified Charnock  
 440 relation—enhances angular momentum dissipation and reduces wind speeds despite a stronger pressure gradient. Figure 12

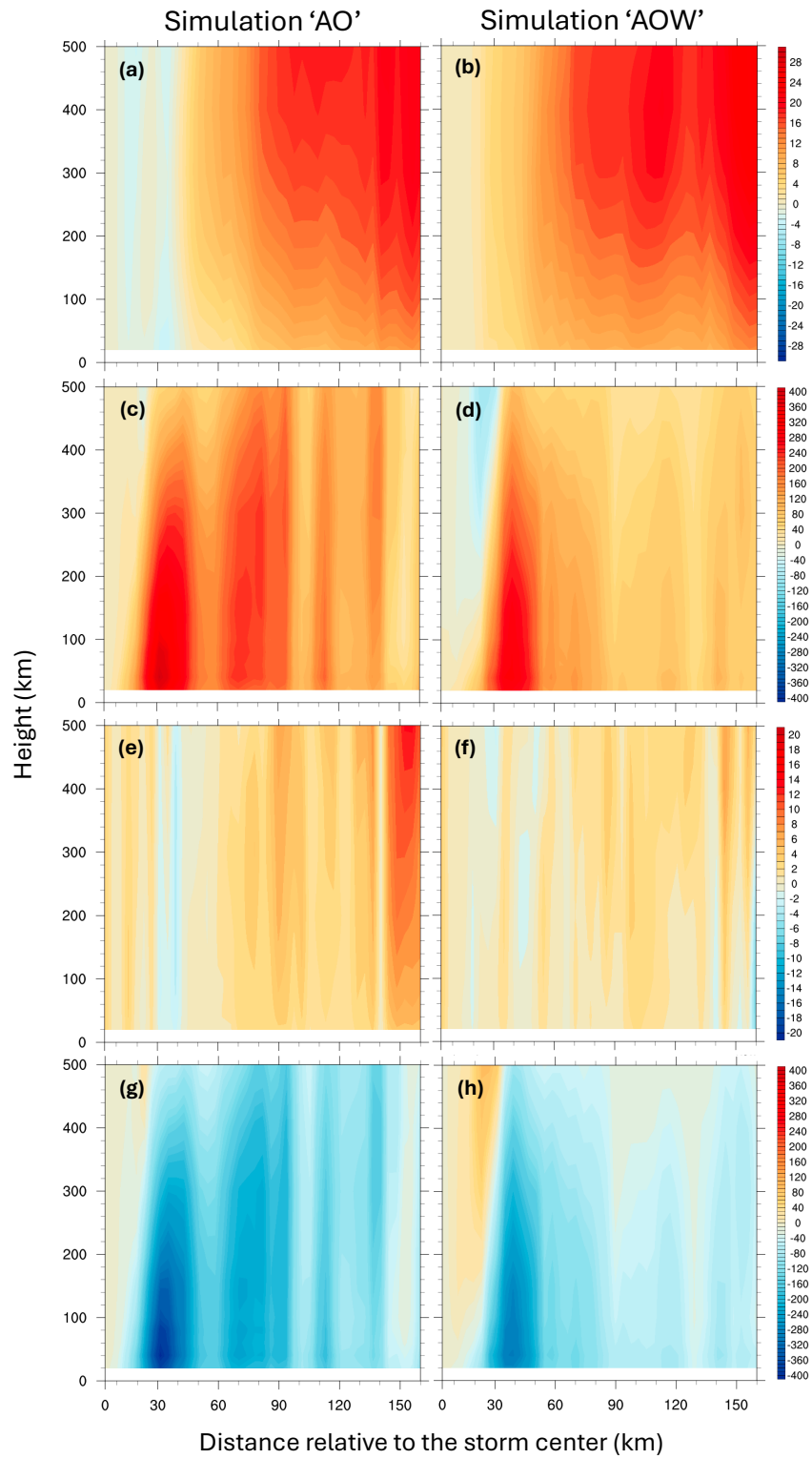
441 presents the AAM tendency, mean radial advection, mean radial eddy transport, and  $F_r$  terms over the period from 00 UTC to  
 442 12 UTC on 22 August 2021, during which both storms underwent steady intensification. The results indicate that the mean  
 443 radial advection (Figure 12b, f) and  $F_r$  (Figure 12d, h) terms are particularly influential in determining the AAM tendency and  
 444 tend to oppose each other. Within 100 km of the storm center, substantial AAM dissipation is observed in the  $F_r$  term for both  
 445 simulations (Figure 12d, h), aligning spatially with regions of elevated  $Z_0$ . However, this dissipation is much more pronounced  
 446 in ‘AO’ (Figure 12d), suggesting that its higher  $Z_0$  values may unrealistically amplify angular momentum loss, leading to  
 447 weaker surface winds despite lower minimum SLP. These findings highlight the crucial role of air-sea interactions, particularly  
 448 those induced by waves and related processes, in accurately simulating the wind structure of TCs within the marine boundary  
 449 layer which impact offshore wind turbines.

450

451 **Table 4. Spatially averaged metrics within 10–60 km of the storm center, vertically integrated through the boundary layer up to 1.2**  
 452 **km above the ground level, at 12 UTC on 22 August 2021. PGF indicates pressure gradient force and is calculated at mean sea level.**

Experiment	BL inflow mass flux ( $\text{kg m}^{-3}$ )	BL vertical mass flux ( $\text{kg m}^{-3}$ )	BL AAM ( $\text{m}^2 \text{s}^{-1}$ )	PGF ( $\text{m s}^{-2}$ )
AO	$1.93 \times 10^4$	$1.34 \times 10^3$	$1.55 \times 10^{10}$	$-1.52 \times 10^2$
AOW	$1.80 \times 10^4$	$1.33 \times 10^3$	$1.61 \times 10^{10}$	$-1.46 \times 10^2$

453



455 **Figure 12. Radius-height plots of the terms in the azimuthally averaged absolute angular momentum budget: (a)-(b) time tendency**  
456 **term ( $\text{m}^2 \text{s}^{-2}$ ), (b) mean advection term ( $\text{m}^2 \text{s}^{-2}$ ), (c) eddy transport term ( $\text{m}^2 \text{s}^{-2}$ ), and (d) friction ( $\text{m}^2 \text{s}^{-2}$ ) and residual during the time**  
457 **from 00 UTC to 12 UTC 22 August 2021. The left column is derived from ‘AO’ and the right column from ‘AOW.’**

## 458 **6 Summary and Discussion**

459 Previous studies of TC wind fields and their impacts on offshore wind turbines have primarily relied on atmosphere-only or  
460 empirical models, which neglect critical interactions among the atmosphere, ocean, and waves. This limitation hampers the  
461 accuracy of risk assessments for offshore wind infrastructure, particularly in hurricane-prone regions. This study developed a  
462 fully coupled modeling system (C-WFS) integrating WRF, FVCOM, and SWAN to simulate atmosphere-ocean-wave  
463 feedback on TC development and assess implications for offshore infrastructure. Using Hurricane Henri (2021) as a case study,  
464 chosen for its impact on the U.S. Northeast and available airborne observations, we ran three experiments of increasing  
465 complexity: ‘A’, ‘AO’, and ‘AOW.’ These were evaluated against observations. All simulations overestimated intensity in  
466 terms of minimum SLP, but the fully coupled ‘AOW’ reduced this bias during development and weakening stages. ‘AOW’  
467 also better captured 3D storm structure, especially low-level winds critical to coastal and offshore energy infrastructure. This  
468 improvement is attributed to wave-induced ocean mixing (cooling SST) and reduced surface roughness, resulting in more  
469 realistic wind fields and lower frictional loss of angular momentum. In contrast, ‘AO’, which lacks wave coupling, exhibited  
470 excessive surface roughness from simplified wind only dependent parameterization, causing greater frictional dissipation and  
471 weaker tangential winds despite a deeper central pressure. These results highlight the importance of including wave dynamics  
472 and incorporating dynamic and thermodynamic feedback among all three components for accurate TC intensity and structural  
473 forecasts.

474 The model also captures wind-wave misalignment and alignment, key processes often overlooked but crucial for evaluating  
475 structural loads, fatigue, and operational risks. Together, these enhancements yield a more realistic representation of storm  
476 evolution, intensity, and structure, underscoring the importance of fully coupled modeling systems for accurate risk  
477 assessments and the development of resilient offshore wind infrastructure.

478 While this study applied C-WFS framework to Category 1 Hurricane Henri and highlighted the role of air-sea interactions in  
479 TC structure and intensity, it has not yet been applied to stronger storms or included sea spray effects, both of which are current  
480 limitations we are actively addressing. A key motivation behind this work is to better understand how coupled dynamics  
481 modulate TC wind fields across different intensities, particularly in regions with offshore wind farms, where storm structure  
482 and intensity can directly affect turbine loading, resilience, and operational risk.

483 Another open question is how the horizontal resolution of ocean components influences TC development in coupled models.  
484 While it is well established that finer atmospheric resolution improves storm intensity forecasts (e.g., Gentry and Lakmann,  
485 2010; Prein et al., 2015), the effects of ocean resolution are less understood. Higher-resolution ocean grids can better resolve  
486 mesoscale and submesoscale features such as eddies and fronts, which influence SST patterns, air-sea fluxes, and upper-ocean  
487 mixing—factors critical to storm intensity and evolution (Zhang et al., 2023). These processes modulate SST cooling and  
488 ocean heat content redistribution during storm passage. Unlike traditional nested-grid approaches (e.g., in COAWST), C-WFS

489 uses an unstructured mesh that smoothly transitions across resolutions, avoiding boundary artifacts. This flexibility makes C-  
490 WFS particularly well suited to explore how ocean resolution affects coupled dynamics and TC behavior—an area we aim to  
491 investigate in future work.

492 In parallel, this modeling framework presents a valuable opportunity to assess whether current IEC (2019a, 2019b) standards  
493 for wind conditions, such as wind shear, veer, and turbulence are adequate for regions prone to TCs. We are currently  
494 performing a comprehensive analysis using this fully coupled model to characterize the representation of these wind parameters,  
495 potentially informing revisions to design criteria that improve the structural resilience and reliability of offshore wind turbines  
496 under TC-induced loading conditions.

497

498 **Code and data availability.** The WRF model (Version 4.5.1) is described by Skamarock et al. (2019), and its code is publicly  
499 available from <https://github.com/wrf-model/WRF> (University Corporation for Atmospheric Research, 2019). The code for  
500 FVCOM (Version 4.3.1., Chen et al., 2003, 2013) for ocean circulation model is publicly available at  
501 <https://github.com/FVCOM-GitHub/fvcom>. The SWAN (Version 41.01, Booij et al., 1999) is a third-generation spectral wave  
502 model developed at Delft University of Technology that computes random, short-crested wind-generated waves in coastal  
503 regions and inland waters (<http://swanmodel.sourceforge.net/>). HYbrid Coordinate Ocean Model (HYCOM; Cummings and  
504 Smedstad, 2014) analysis data used for ocean model forcing is available at <http://hycom.org/dataserver/>. NCEP provides  
505 Global Forecast System (GFS; NCEP, 2015) data, which is used as atmospheric forcing data, available at  
506 <https://www.nco.ncep.noaa.gov/pmb/products/gfs/>. The OSTIA (Good et al., 2020) global sea surface temperature provides  
507 daily maps of foundation sea surface temperature at  $0.05^\circ \times 0.05^\circ$  available from  
508 [https://data.marine.copernicus.eu/product/SST\\_GLO\\_SST\\_L4\\_REP\\_OBSERVATIONS\\_010\\_011/description](https://data.marine.copernicus.eu/product/SST_GLO_SST_L4_REP_OBSERVATIONS_010_011/description). The NCL and  
509 Python codes for performing analysis and visualization are available at <https://www.ncl.ucar.edu/> and  
510 <https://www.python.org/downloads/>, respectively. All simulation data are available from the Wind Data Hub: Wang, J. (2021):  
511 High-Resolution Regional Atmosphere–Ocean–Wave Coupled Simulations of Hurricane Henri (2021), U.S. Department of  
512 Energy, Office of Energy Efficiency and Renewable Energy [data set], <https://doi.org/10.21947/3019326>, last access: 17  
513 March 2026.

514

515 **Author contribution.** Conceptualization, Formal analysis, Validation, Visualization: CJ, JW, PX, CH, WP; Data curation,  
516 Investigation, Software: CJ, JW, CH, MB, GN; Funding acquisition, Resources, Supervision: JW, PX, WP; Methodology: CJ,  
517 CH, WP; Project administration: JW, PX; Writing – original draft: CJ, JW, PX, WP; Writing – review & editing: CJ, JW, PX,  
518 CH, MB, GN.

519

520 **Competing interests.** The authors declare that they have no competing interests.

521

522 **Acknowledgements.** This study is supported by the Wind Energy Technologies Office (WETO) of the U.S. Department of  
523 Energy (DOE) Office of Energy Efficiency and Renewable Energy. The WRF model was made available by the National  
524 Center for Atmospheric Research, which is sponsored by NSF. High-Performance Computing support from the Theta cluster  
525 operated by Argonne Leadership Computing Facility (ALCF) and Kestrel operated by National Renewable Energy Laboratory  
526 (NREL).

527 **References**

- 528 Aijaz, S., Ghantous, M., Babanin, A. V., Ginis, I., Thomas, B., and Wake, G.: Nonbreaking wave-induced mixing in upper  
529 ocean during tropical cyclones using coupled hurricane-ocean-wave modeling, *Journal of Geophysical Research: Oceans*,  
530 122, 3939–3963, <https://doi.org/10.1002/2016JC012586>, 2017.
- 531 Akinsanola, A. A., Jung, C., Wang, J., and Kotamarthi, V. R.: Evaluation of precipitation across the contiguous United  
532 States, Alaska, and Puerto Rico in multi-decadal convection-permitting simulations, *Scientific Reports*, 14, 1238, 2024.
- 533 Arthur, W. C.: A statistical–parametric model of tropical cyclones for hazard assessment, *Natural Hazards and Earth System  
534 Sciences*, 21, 893–916, <https://doi.org/10.5194/nhess-21-893-2021>, 2021.
- 535 Barr, B. W. and Chen, S. S.: Impacts of seastate-dependent sea spray heat fluxes on tropical cyclone structure and intensity  
536 in fully coupled atmosphere-wave-ocean model simulations, *Journal of Advances in Modeling Earth Systems*, 17,  
537 e2024MS004550. <https://doi.org/10.1029/2024MS004550>, 2024.
- 538 Booij, N., Ris, R. C., and Holthuijsen, L. H.: A third-generation wave model for coastal regions. Part I: Model description  
539 and validation, *Journal of Geophysical Research*, 104, 7649–7666, <https://doi.org/10.1029/98JC02622>, 1999.
- 540 Charnock, H., 1955: Wind stress on a water surface. *Quart. J. Roy. Meteor. Soc.*, 81, 639–640.
- 541 Chen, C., Beardsley, R. C., and Cowles, G.: An unstructured grid, finite-volume coastal ocean model: FVCOM user manual,  
542 Technical Report SMAST/UMASSD-13-0701, 416 pp., 2013.
- 543 Chen, C., Liu, H., and Beardsley, R. C.: An unstructured grid, finite-volume, three-dimensional, primitive equations ocean  
544 model: Application to coastal ocean and estuaries, *Journal of Atmospheric and Oceanic Technology*, 20, 159–186,  
545 [https://doi.org/10.1175/1520-0426\(2003\)020<0159:AUGFVT>2.0.CO;2](https://doi.org/10.1175/1520-0426(2003)020<0159:AUGFVT>2.0.CO;2), 2003.
- 546 Chen, P., Zhang, Z., Li, Y., Ye, R., Li, R., and Song, Z.: The two-parameter Holland pressure model for tropical cyclones,  
547 *Journal of Marine Science and Engineering*, 12, 92, <https://doi.org/10.3390/jmse12010092>, 2024.
- 548 Chen, S. S., Price, J. F., Zhao, W., Donelan, M. A., and Walsh, E. J.: The CBLAST-hurricane program and the next-  
549 generation fully coupled atmosphere–wave–ocean models for hurricane research and prediction, *Bulletin of the American  
550 Meteorological Society*, 88, 311–318, 2007.
- 551 Chen, S. S., Zhao, W., Donelan, M. A., and Tolman, H. L.: Directional wind–wave coupling in fully coupled atmosphere–  
552 wave–ocean models: Results from CBLAST-Hurricane, *Journal of the Atmospheric Sciences*, 70, 3198–3215, 2013.
- 553 Craig, A., Valcke, S., and Coquart, L.: Development and performance of a new version of the OASIS coupler, OASIS3-  
554 MCT\_3.0, *Geoscientific Model Development*, 10, 3297–3308, <https://doi.org/10.5194/gmd-10-3297-2017>, 2017.
- 555 Creasey, R. L., and Elsberry, R. L.: Tropical cyclone center positions from sequences of HDSS sondes deployed along high-  
556 altitude overpasses. *Wea. Forecasting*, 32, 317–325, <https://doi.org/10.1175/WAF-D-16-0096.1>, 2017.
- 557 Cummings, J. A. and Smedstad, O. M.: Ocean data impacts in global HYCOM, *Journal of Atmospheric and Oceanic  
558 Technology*, 31, 1771–1791, <https://doi.org/10.1175/JTECH-D-14-00011.1>, 2014.
- 559 DeMaria, M., Knaff, J. A., and Sampson, C.: Evaluation of long-term trends in tropical cyclone intensity forecasts,  
560 *Meteorology and Atmospheric Physics*, 97, 19–28, 2007.
- 561 DeMaria, M., Sampson, C. R., Knaff, J. A., and Musgrave, K. D.: Is tropical cyclone intensity guidance improving?, *Bulletin  
562 of the American Meteorological Society*, 95, 387–398, <https://doi.org/10.1175/bams-d-12-00240.1>, 2014.

563 Donelan, M. A. et al. On the limiting aerodynamic roughness of the ocean in very strong winds. *Geophys. Res. Lett.* 31,  
564 L18306, 10.1029/2004GL019460, 2004.

565 Drennan, W. M., Graber, H. C., Hauser, D., and Quentin, C.: On the wave age dependence of wind stress over pure wind  
566 seas, *Journal of Geophysical Research: Oceans*, 108, 8062, 2003.

567 Drennan, W. M., Taylor, P. K., and Yelland, M. J., “Parameterizing the sea surface roughness,” *J. Phys. Oceanogr.* 35(5),  
568 835–848, 2005.

569 Dyer, A. J. and Hicks, B. B.: Flux-gradient relationships in the constant flux layer, *Quarterly Journal of the Royal*  
570 *Meteorological Society*, 96, 715–721, 1970.

571 Emanuel, K. A.: An air-sea interaction model of the tropical cyclones. Part I: Steady-State Maintenance, *Journal of the*  
572 *Atmospheric Sciences*, 43, 585–605, [https://doi.org/10.1175/1520-0469\(1986\)043<0585:AASITF>2.0.CO;2](https://doi.org/10.1175/1520-0469(1986)043<0585:AASITF>2.0.CO;2), 1986.

573 Fan, Y., Ginis, I., and Hara, T.: The effect of wind–wave–current interaction on air–sea momentum fluxes and ocean  
574 response in tropical cyclones, *Journal of Physical Oceanography*, 39, 1019–1034, 2009.

575 Fischer, M. S., Reasor, P. D., Rogers, R. F., and Gamache, J. F.: An analysis of tropical cyclone vortex and convective  
576 characteristics in relation to storm intensity using a novel airborne doppler radar database, *Monthly Weather Review*, 150,  
577 2255–2278, <https://doi.org/10.1175/MWR-D-21-0223.1>, 2022.

578 Gentry, M. A. and Lackmann, G. M.: Sensitivity of simulated tropical cyclone structure and intensity to horizontal resolution,  
579 *Monthly Weather Review*, 138, 688–704, 2010.

580 Ghantous, M. and Babanin, A. V.: One-dimensional modeling of upper ocean mixing by turbulence due to wave orbital  
581 motion, *Nonlinear Processes in Geophysics*, 21, 325–338, <https://doi.org/10.5194/npg-21-325-2014>, 2014a.

582 Ghantous, M. and Babanin, A. V.: Ocean mixing by wave orbital motion, *Acta Physica Slovaca*, 64, 1–57,  
583 <https://doi.org/10.2478/apsrt-2014-0001>, 2014b.

584 Good, S., Fiedler, E., Mao, C., Martin, M. J., Maycock, A., Reid, R., Roberts-Jones, J., Searle, T., Waters, J., While, J., and  
585 Worsfold, M.: The current configuration of the OSTIA system for operational production of foundation sea surface  
586 temperature and ice concentration analyses, *Remote Sensing*, 12, 720, <https://doi.org/10.3390/rs12040720>, 2020.

587 Hong, S.-Y. and Lim, J.-O.: The WRF single-moment 6-class microphysics scheme (WSM6), *Journal of the Korean*  
588 *Meteorological Society*, 42, 129–151, 2006.

589 Hong, S.-Y., Noh, Y., and Dudhia, J.: A new vertical diffusion package with an explicit treatment of entrainment processes,  
590 *Monthly Weather Review*, 134, 2318–2341, 2006.

591 Iacono, M. J., Delamere, J. S., Mlawer, E. J., Shephard, M. W., Clough, S. A., and Collins, W. D.: Radiative forcing by  
592 long-lived greenhouse gases: Calculations with the AER radiative transfer models, *Journal of Geophysical Research*, 113,  
593 D13103, <https://doi.org/10.1029/2007JD009277>, 2008.

594 IEC: Wind turbines - part 1: Design requirements (No. IEC 61400-1:2019), 2019a.

595 IEC: Wind turbines – part 3: Design requirements for offshore wind turbines (No. IEC 61400-3-1:2019), 2019b

596 Itiki, R., Manjrekar, M., Di Santo, S. G., and Itiki, C.: Method for spatiotemporal wind power generation profile under  
597 hurricanes: US-Caribbean super grid proposition, *Renewable and Sustainable Energy Reviews*, 173, 113082, 2023.

598 Jimenez, P., Dudhia, J., Gonzalez-Ruoco, J. F., Navarro, J., Montavez, J. P., and Garcia-Bustamente, E.: A revised scheme  
599 for the WRF surface layer formulation, *Monthly Weather Review*, 140, 898–918, 2012.

600 Knapp, K. R., Kruk, M. C., Levinson, D. H., Diamond, H. J., and Neumann, C. J.: The international best track archive for  
601 climate stewardship (IBTrACS) unifying tropical cyclone data, *Bulletin of the American Meteorological Society*, 91, 363–  
602 376, 2010.

603 Komen, G. J., Hasselmann, K., and Hasselmann, S.: On the existence of a fully developed wind-sea spectrum, *Journal of*  
604 *Physical Oceanography*, 14, 1271–1285, [https://doi.org/10.1175/1520-0485\(1984\)014<1271:OTEOAF>2.0.CO;2](https://doi.org/10.1175/1520-0485(1984)014<1271:OTEOAF>2.0.CO;2), 1984.

605 Kouadio, K., Bastin, S., Konare, A., and Ajayi, V. O.: Does convection-permitting simulate better rainfall distribution and  
606 extreme over Guinean coast and surroundings?, *Climate Dynamics*, 55, 153–174, [https://doi.org/10.1007/s00382-018-](https://doi.org/10.1007/s00382-018-4308-y)  
607 4308-y, 2020.

608 Ma, T. and Sun, C.: Large Eddy Simulation of Combined Wind-wave Loading on Offshore Wind Turbines, arXiv [preprint],  
609 arXiv:2310.03407, 2023.

610 Madsen, O. S., Poon, Y. K., and Graber, H. C.: Spectral wave attenuation by bottom friction: Theory, in: *Proceedings of the*  
611 *International Conference on Coastal Engineering*, 21, 492–506, 1988.

612 Mellor, G. L. and Yamada, T.: Development of a turbulence closure model for geophysical fluid problems, *Reviews of*  
613 *Geophysics*, 20, 851–875, <https://doi.org/10.1029/RG020i004p00851>, 1982.

614 Nakanishi, M. and Niino, H.: Development of an improved turbulence closure model for the atmospheric boundary layer,  
615 *Journal of the Meteorological Society of Japan*, 87, 895–912, <https://doi.org/10.2151/jmsj.87.895>, 2009.

616 National Data Buoy Center (NDBC), NOAA: National Data Buoy Center (NDBC) Moored Buoy and C-MAN Station Data,  
617 UCAR/NCAR - Earth Observing Laboratory, <https://doi.org/10.26023/V640-H29S-MR0S>, 2008.

618 National Centers for Environmental Prediction (NCEP): NCEP GFS 0.25 Degree Global Forecast Grids Historical Archive,  
619 Research Data Archive at the National Center for Atmospheric Research, Computational and Information Systems  
620 Laboratory, <https://doi.org/10.5065/D65D8PWK>, 2015.

621 Olson, J. B., Kenyon, J. S., Angevine, W. M., Brown, J. M., Pagowski, M., and Sušelj, K.: A description of the MYNN-  
622 EDMF scheme and coupling to other components in WRF-ARW, NOAA Technical Memorandum OAR GSD No. 61, 37  
623 pp., <https://doi.org/10.25923/n9wm-be49>, 2019.

624 Paulson, C. A.: The mathematical representation of wind speed and temperature profiles in the unstable atmospheric surface  
625 layer, *Journal of Applied Meteorology*, 9, 857–861, 1970.

626 Powell, M. D., Vickery, P. J. & Reinhold, T. A. Reduced drag coefficient for high wind speeds in tropical cyclones. *Nature*  
627 422, 279–283, 2003.

628 Prein, A. F., Langhans, W., Fosser, G., Ferrone, A., Ban, N., Goergen, K., Keller, M., Tölle, M., Gutjahr, O., Feser, F., et  
629 al.: A review on regional convection-permitting climate modeling: Demonstrations, prospects, and challenges, *Reviews*  
630 *of Geophysics*, 53, 323–361, <https://doi.org/10.1002/2014RG000475>, 2015.

631 Pringle, W. J. and Kotamarthi, V. R.: Coupled ocean wave-atmosphere models for offshore wind energy, Argonne National  
632 Laboratory, <https://doi.org/10.2172/1829093>, 2021.

633 Qing, Y. and Wang, S.: Multi-decadal convection-permitting climate projections for China’s Greater Bay Area and  
634 surroundings, *Climate Dynamics*, <https://doi.org/10.1007/s00382-021-05716-w>, 2021.

635 Rappaport, E. N., et al.: Advances and challenges at the National Hurricane Center, *Weather and Forecasting*, 24, 395–419,  
636 2009.

637 Roldán, M., Montoya, R. D., Rios, J. D., and Osorio, A. F.: Modified parametric hurricane wind model to improve the  
638 asymmetry in the region of maximum winds, *Ocean Engineering*, 280, 114508,  
639 <https://doi.org/10.1016/j.oceaneng.2023.114508>, 2023.

640 Sanchez Gomez, M., Lundquist, J. K., Mirocha, J. D., and Arthur, R. S.: Investigating the physical mechanisms that modify  
641 wind plant blockage in stable boundary layers, *Wind Energy Science*, 8, 1049–1069, [https://doi.org/10.5194/wes-8-1049-](https://doi.org/10.5194/wes-8-1049-2023)  
642 2023, 2023.

643 Schade, L. R. and Emanuel, K. A.: The ocean's effect on the intensity of tropical cyclones: Results from a simple coupled  
644 atmosphere–ocean model, *Journal of the Atmospheric Sciences*, 56, 642–651, 1999.

645 Shanahan, T. and Fitzgerald, B.: Wind–Wave Misalignment in Irish Waters and Its Impact on Floating Offshore Wind  
646 Turbines. *Energies*, 18(2), 372; <https://doi.org/10.3390/en18020372>, 2025.

647 Shimura, T., Noh, Y., and Hara, T.: Long-term impacts of ocean wave-dependent roughness on global climate systems, *J.*  
648 *Geophys. Research: Oceans*, 122(3), 1995–2011, <https://doi.org/10.1002/2016JC012621>, 2017.

649 Skamarock, W. C., Klemp, J. B., Dudhia, J., Gill, D. O., Liu, Z., Berner, J., Wang, W., Powers, J. G., Duda, M. G., and  
650 Barker, D. M.: A description of the advanced research WRF model version 4, 145 pp., National Center for Atmospheric  
651 Research, 2019.

652 Smagorinsky, J.: General circulation experiments with the primitive equations, part I: the basic experiment, *Monthly*  
653 *Weather Review*, 91, 99–164, 1963.

654 Smith, A. B.: 2010–2019: A landmark decade of U.S. billion-dollar weather and climate disasters, NOAA,  
655 [https://www.climate.gov/news-features/blogs/beyond-data/2010-2019-landmark-decade-us-billion-dollar-weather-and-](https://www.climate.gov/news-features/blogs/beyond-data/2010-2019-landmark-decade-us-billion-dollar-weather-and-climate)  
656 [climate](https://www.climate.gov/news-features/blogs/beyond-data/2010-2019-landmark-decade-us-billion-dollar-weather-and-climate), 2020.

657 Sun, X., Xue, M., Brotzge, J., McPherson, R. A., Hu, X.-M., and Yang, X.-Q.: An evaluation of dynamical downscaling of  
658 Central Plains summer precipitation using a WRF-based regional climate model at a convection-permitting 4 km  
659 resolution, *Journal of Geophysical Research: Atmospheres*, 121, 13801–13825, <https://doi.org/10.1002/2016JD024796>,  
660 2016.

661 Taylor, P. K. and Yelland, M. J.: The dependence of sea surface roughness on the height and steepness of the waves, *Journal*  
662 *of Physical Oceanography*, 31, 572–590, 2001.

663 Wada, A. and Usui, N.: Impacts of oceanic preexisting conditions on predictions of Typhoon Hai-Tang in 2005, *Advances*  
664 *in Meteorology*, 2010, 756071, 2010.

665 Warner, J. C., Armstrong, B., He, R., and Zambon, J. B.: Development of a coupled ocean–atmosphere–wave–sediment  
666 transport (COAWST) modeling system, *Ocean Modelling*, 35, 230–244, <https://doi.org/10.1016/j.oceanmod.2010.07.010>,  
667 2010.

668 Webb, E. K.: Profile relationships: The log-linear range, and extension to strong stability, *Quarterly Journal of the Royal*  
669 *Meteorological Society*, 96, 67–90, 1970.

670 Wei, J., Jiang, G. Q., and Liu, X.: Parameterization of typhoon-induced ocean cooling using temperature equation and  
671 machine learning algorithms: An example of Typhoon Soulik (2013), *Ocean Dynamics*, 67, 1179–1193,  
672 <https://doi.org/10.1007/s10236-017-1082-z>, 2017.

673 Wright, C. W., et al.: Hurricane directional wave spectrum spatial variation in the open ocean, *Journal of Physical*  
674 *Oceanography*, 31, 2472–2488, 2001.

675 Wu, L., Rutgersson, A., Sahlée, E., and Guo Larsén, X.: Swell impact on wind stress and atmospheric mixing in a regional  
676 coupled atmosphere-wave model, *Journal of Geophysical Research: Oceans*, 121, 4633–4648,  
677 <https://doi.org/10.1002/2015JC011576>, 2016.

678 Xu, X., Voermans, J. J., Zhang, W., Zhao, B., Qiao, F., Liu, Q., Moon, I.-J., Janekovic, I., Waseda, T., and Babanin, A. V.:  
679 Tropical cyclone modeling with the inclusion of wave-coupled processes: sea spray and wave turbulence, *Geophys. Res.*  
680 *Let.*, 50, e2023GL106536, <https://doi.org/10.1029/2023GL106536>, 2023.

681 Yamaguchi, M., Ishida, J., Sato, H., and Nakagawa, M.: WGNE intercomparison of tropical cyclone forecasts by operational  
682 nwp models: A quarter century and beyond, *Bulletin of the American Meteorological Society*, 98, 2337–2349,  
683 <https://doi.org/10.1175/bams-d-16-0133.1>, 2017.

684 Zambon, J. B., He, R., and Warner, J. C.: Investigation of Hurricane Ivan using the coupled ocean–atmosphere–wave–  
685 sediment transport (COAWST) model, *Ocean Dynamics*, 64, 1535–1554, <https://doi.org/10.1007/s10236-014-0777-7>,  
686 2014.

687 Zambon, J. B., He, R., Warner, J. C., and Hegermiller, C. A.: Impact of SST and surface waves on Hurricane Florence  
688 (2018): A coupled modeling investigation, *Weather and Forecasting*, 36, 1713–1734, [https://doi.org/10.1175/WAF-D-20-](https://doi.org/10.1175/WAF-D-20-0171.1)  
689 [0171.1](https://doi.org/10.1175/WAF-D-20-0171.1), 2021.

690 Zhang, J. A. and Marks, F. D.: Effects of horizontal diffusion on tropical cyclone intensity change and Xd structure in  
691 idealized three-dimensional numerical simulations, *Monthly Weather Review*, 143, 3981–3995,  
692 <https://doi.org/10.1175/mwr-d-14-00341.1>, 2015.

693 Zhang, S., Xu, S., Fu, H., Wu, L., Liu, Z., Gao, Y., et al.: Toward earth system modeling with resolved clouds and ocean  
694 submesoscales on heterogeneous many-core HPCs, *National Science Review*, 10, nwad069, 2023.

695 Zhao, B., Qiao, F., Cavaleri, L., Wang, G., Bertotti, L., and Liu, L.: Sensitivity of typhoon modeling to surface waves and  
696 rainfall, *Journal of Geophysical Research: Oceans*, 122, 1702–1723, <https://doi.org/10.1002/2016JC012262>, 2017.

697 Zhao, B., Wang, G., Zhang, J. A., Liu, L., Liu, J., Xu, J., et al.: The effects of ocean surface waves on tropical cyclone  
698 intensity: Numerical simulations using a regional atmosphere-ocean-wave coupled model, *Journal of Geophysical*  
699 *Research: Oceans*, 127, e2022JC019015, <https://doi.org/10.1029/2022JC019015>, 2022.

700 Zhou, X., Hara, T., Ginis, I., D’Asaro, E., and Reichl, B. G.: Evidence of Langmuir mixing effects in the upper ocean layer  
701 during tropical cyclones using observations and a coupled wave-ocean model, *Journal of Geophysical Research: Oceans*,  
702 128, e2023JC020062, <https://doi.org/10.1029/2023JC020062>, 2023.